The Meteoritical Society

Meteoritics & Planetary Science 1–21 (2024)
doi: 10.1111/maps.14124

Four-dimensional-STEM analysis of the phyllosilicate-rich matrix of Ryugu samples

Bahae-eddine MOULOUD[1], Damien JACOB[1]*, Francisco de la PEÑA[1], Maya MARINOVA[2], Corentin LE GUILLOU[1], Jean-Christophe VIENNET[1], Sylvain LAFORET[1], Hugues LEROUX[1], Adrien TEURTRIE[1], Takaaki NOGUCHI[3], Toru MATSUMOTO[3,4], Akira MIYAKE[3], Yohei IGAMI[3], Mitsutaka HARUTA[5], Hikaru SAITO[6,7], Satoshi HATA[8,9], Yusuke SETO[10], Masaaki MIYAHARA[11], Naotaka TOMIOKA[12], Hope A. ISHII[13], John P. BRADLEY[13], Kenta K. OHTAKI[13], Elena DOBRICA[13], Falko LANGENHORST[14], Dennis HARRIES[15], Pierre BECK[16], Thi H. V. PHAN[16], Rolando REBOIS[16], Neyda M. ABREU[17], Jennifer GRAY[18], Thomas ZEGA[19], Pierre-M. ZANETTA[19], Michelle S. THOMPSON[20], Rhonda STROUD[21], Kate BURGESS[22], Brittany A. CYMES[23], John C. BRIDGES[24], Leon HICKS[24,25], Martin R. LEE[26], Luke DALY[26,27,28], Phil A. BLAND[29], Michael E. ZOLENSKY[30], David R. FRANK[13], James MARTINEZ[31], Akira TSUCHIYAMA[32,33,34], Masahiro YASUTAKE[35], Junya MATSUNO[32], Shota OKUMURA[3], Itaru MITSUKAWA[3], Kentaro UESUGI[35], Masayuki UESUGI[35], Akihisa TAKEUCHI[35], Mingqi SUN[33,34,36], Satomi ENJU[37], Aki TAKIGAWA[38], Tatsuhiro MICHIKAMI[39], Tomoki NAKAMURA[40], Megumi MATSUMOTO[40], Yusuke NAKAUCHI[41], Masanao ABE[41,42], Satoru NAKAZAWA[41], Tatsuaki OKADA[41,42], Takanao SAIKI[41], Satoshi TANAKA[41,42], Fuyuto TERUI[43], Makoto YOSHIKAWA[41,42], Akiko MIYAZAKI[41], Aiko NAKATO[41], Masahiro NISHIMURA[41], Tomohiro USUI[41], Toru YADA[41], Hisayoshi YURIMOTO[44], Kazuhide NAGASHIMA[13], Noriyuki KAWASAKI[44], Naoya SAKAMOTOA[45], Ryuji OKAZAKI[46], Hikaru YABUTA[11], Hiroshi NARAOKA[46], Kanako SAKAMOTO[41], Shogo TACHIBANA[47], Sei-ichiro WATANABE[48], and Yuichi TSUDA[41]

[1]CNRS, INRAE, Centrale Lille, UMR 8207-UMET-Unité Matériaux et Transformations, Université de Lille, Villeneuve d'Ascq, France
[2]CNRS, INRAE, Centrale Lille, Université Artois, FR 2638-IMEC-Institut Michel-Eugène Chevreul, Université de Lille, Villeneuve d'Ascq, France
[3]Division of Earth and Planetary Sciences, Kyoto University, Kyoto, Japan
[4]The Hakubi Center for Advanced Research, Kyoto University, Kyoto, Japan
[5]Institute for Chemical Research, Kyoto University, Kyoto, Japan
[6]Institute for Materials Chemistry and Engineering, Kyushu University, Fukuoka, Japan
[7]Pan-Omics Data-Driven Research Innovation Center, Kyushu University, Fukuoka, Japan
[8]Interdisciplinary Graduate School of Engineering Sciences, Kyushu University, Fukuoka, Japan
[9]The Ultramicroscopy Research Center, Kyushu University, Fukuoka, Japan
[10]Department of Geosciences, Osaka Metropolitan University, Osaka, Japan
[11]Department of Earth and Planetary Systems Science, Hiroshima University, Hiroshima, Japan
[12]Kochi Institute for Core Sample Research, X-Star, JAMSTEC, Nankoku, Japan
[13]Hawai'i Institute of Geophysics and Planetology, The University of Hawai'i at Mānoa, Honolulu, Hawaii, USA
[14]Institut für Geowissenschaften, Friedrich-Schiller-Universität Jena, Jena, Germany
[15]European Space Resources Innovation Centre, Luxembourg Institute of Science and Technology, Belvaux, Luxembourg
[16]Institut de Planétologie et d'Astrophysique de Grenoble (IPAG), CNRS, Université Grenoble Alpes, Grenoble, France
[17]NASA Langley Research Center, Hampton, Virginia, USA
[18]Materials Characterization Lab, The Pennsylvania State University Materials Research Institute, University Park, Pennsylvania, USA
[19]Lunar and Planetary Laboratory, Department of Planetary Sciences, The University of Arizona, Tucson, Arizona, USA
[20]Department of Earth, Atmospheric and Planetary Sciences, Purdue University, West Lafayette, Indiana, USA
[21]Buseck Center for Meteorite Studies, Arizona State University, Tempe, Arizona, USA
[22]Materials Science and Technology Division, U.S. Naval Research Laboratory, Washington, DC, USA
[23]U.S. Naval Research Laboratory, Washington, DC, USA

[24]Space Park Leicester, University of Leicester, Leicester, UK
[25]School of Geology, Geography and the Environment, University of Leicester, Leicester, UK
[26]School of Geographical and Earth Sciences, The University of Glasgow, Glasgow, UK
[27]Australian Centre for Microscopy and Microanalysis, The University of Sydney, Sydney, New South Wales, Australia
[28]Department of Materials, The University of Oxford, Oxford, UK
[29]School of Earth and Planetary Sciences, Curtin University, Perth, Western Australia, Australia
[30]ARES, NASA Johnson Space Center, Houston, Texas, USA
[31]Jacobs Engineering, Dallas, Texas, USA
[32]Research Organization of Science and Technology, Ritsumeikan University, Kusatsu, Japan
[33]CAS Key Laboratory of Mineralogy and Metallogeny, Guangdong Provincial Key Laboratory of Mineral Physics and Materials, Guangzhou Institute of Geochemistry, Chinese Academy of Sciences (CAS), Guangzhou, China
[34]CAS Center for Excellence in Deep Earth Science, Guangzhou, China
[35]Japan Synchrotron Radiation Research Institute, Sayo-gun, Japan
[36]University of Chinese Academy of Sciences, Beijing, China
[37]Department of Mathematics, Physics, and Earth Science, Ehime University, Matsuyama, Japan
[38]Department of Earth and Planetary Science, The University of Tokyo, Tokyo, Japan
[39]Faculty of Engineering, Kindai University, Hiroshima, Japan
[40]Department of Earth Science, Tohoku University, Sendai, Japan
[41]Institute of Space and Astronautical Science, Japan Aerospace Exploration Agency, Sagamihara, Japan
[42]The Graduate University for Advanced Studies, SOKENDAI, Hayama, Japan
[43]Department of Mechanical Engineering, Kanagawa Institute of Technology, At-sugi, Japan
[44]Department of Earth and Planetary Sciences, Hokkaido University, Sapporo, Japan
[45]Creative Research Institution Sousei, Hokkaido University, Sapporo, Japan
[46]Department of Earth and Planetary Sciences, Kyushu University, Fukuoka, Japan
[47]Tokyo Organization for Planetary and Space Science, The University of Tokyo, Tokyo, Japan
[48]Department of Earth and Environmental Sciences, Nagoya University, Nagoya, Japan
***Correspondence**
Damien Jacob, CNRS, INRAE, Centrale Lille, UMR 8207-UMET-Unité Matériaux et Transformations, Université de Lille, Lille F-59000, France.
Email: damien.jacob@univ-lille.fr

(Received 08 June 2023; revision accepted 14 December 2023)

Abstract–Ryugu asteroid grains brought back to the Earth by the Hayabusa2 space mission are pristine samples containing hydrated minerals and organic compounds. Here, we investigate the mineralogy of their phyllosilicate-rich matrix with four-dimensional scanning transmission electron microscopy (4D-STEM). We have identified and mapped the mineral phases at the nanometer scale (serpentine, smectite, pyrrhotite), observed the presence of Ni-bearing pyrrhotite, and identified the serpentine polymorph as lizardite, in agreement with the reported aqueous alteration history of Ryugu. Furthermore, we have mapped the d-spacings of smectite and observed a broad distribution of values, ranging from 1 to 2 nm, with an average d-spacing of 1.24 nm, indicating significant heterogeneity within the sample. Such d-spacing variability could be the result of either the presence of organic matter trapped in the interlayers or the influence of various geochemical conditions at the submicrometer scale, suggestive of a range of organic compounds and/or changes in smectite crystal chemistry.

INTRODUCTION

Samples from the C-type (carbonaceous) asteroid 162173 Ryugu were returned to the Earth by the Hayabusa2 space mission of the Japanese Aerospace Exploration Agency (JAXA). Recent studies report that Ryugu belongs to the CI (Ivuna-like) group of chondrites. Whereas Ryugu grains have experienced space weathering (Noguchi et al., 2023) they have never witnessed terrestrial weathering effects, making them the most fresh and uncontaminated CI chondrites studied so far (e.g., Ito et al., 2022; Nakamura et al., 2023; Yada et al., 2022; Yokoyama et al., 2022). This high level of preservation makes Ryugu samples particularly valuable for understanding

the composition and evolution of the early solar system and the transformations of solid matter on small carbonaceous asteroids, as well as for developing new analytical techniques that can be applied to future sample return missions. Mineralogical investigations have revealed that Ryugu grains are composed mainly of phyllosilicates (a mixture of serpentine and smectite), magnetites, Fe-sulfides, and carbonates (e.g., Ito et al., 2022; Nakamura et al., 2023; Viennet et al., 2023; Yamaguchi et al., 2023). The presence of phyllosilicates in Ryugu grains, which are also common in many carbonaceous chondrites (CCs) (e.g., Brearley, 2006; Clayton & Mayeda, 1984), shows that Ryugu has undergone aqueous alteration (Nakamura et al., 2023). Transmission electron microscopy (TEM) analyses have found out that the fine-grained materials at the nanometer scale are predominantly phyllosilicates, nanosulfides, and organic matter (Ito et al., 2022; Leroux et al., this issue; Noguchi et al., this issue), while coarser materials ($\sim >10$ μm) are mostly magnetite, iron sulfides, and carbonates (e.g., Dobrică et al., 2023; Nakamura et al., 2023; Yokoyama et al., 2022). Previous studies have also shown that Ryugu's samples' phyllosilicate-rich matrix is composed of multiple lithologies (Nakamura et al., 2023), showing heterogeneous elemental and isotopic distributions (e.g., H, B, C, N, and Na).

A variety of analysis techniques have been employed in order to characterize the mineralogy of the phyllosilicate-rich matrix (PSM) in carbonaceous chondrites in the last few decades, most of which were used in recent studies of Ryugu grains. The bulk characteristics of CCs have been investigated by transmission infrared spectroscopy (IR) in the (2–25 μm) spectral range, providing a classification method of CCs and a way to determine the nature of their phyllosilicates (Beck et al., 2014). X-ray diffraction provided a basis for petrologic classification of CCs (Howard et al., 2009, 2011), allowed accurate quantification of their modal mineralogy, and enabled the estimation of the degree of aqueous alteration primarily from the abundance of phyllosilicates (Howard et al., 2009, 2011; King et al., 2015, 2017).

TEM studies have revealed the heterogeneous nature of CCs and the nanometer scale mixing between phases (Barber, 1981; Brearley, 2006; Nakamura et al., 2023; Tomeoka & Buseck, 1988; Yokoyama et al., 2022). The ease with which TEM provides petrographical and mineralogical information at a scale where phyllosilicates can be distinguished from other matrix constituents has led to its widespread application in the study of chondritic materials. High-resolution transmission electron microscopy (HRTEM), due to its high magnification, is suitable to study in detail small regions of interest of the sample. It has been used to distinguish between the various phyllosilicates found in chondrites such as the CI chondrite Orgueil (Tomeoka & Buseck, 1988), the Yamato-74662 carbonaceous chondrite (Akai, 1982), the Mighei-type carbonaceous (CM) chondrites ALH-81002 and Bells (Brearley, 1995; Lauretta et al., 2000), and, most recently, the Ryugu asteroid samples (Nakamura et al., 2023; Noguchi et al., this issue). Selected area electron diffraction (SAED) has been employed in chondritic materials for structural analysis (Barber, 1981; Marinova et al., 2021; Trigo-Rodríguez et al., 2019). However, the amount of information that can be obtained from SAED is constrained by the fine-grained nature, the thickness changes of individual crystallites, their variable degree of crystallinity, and most importantly, by the size of the selected area ($\sim$100 nm and higher), which is one order of magnitude larger than typical particle sizes (Ferrell & Paulson, 1977). When the grain size is large enough (around 100 nm) and no overlapping occurs, the recently developed 3-D precession electron diffraction (3-D-PED) is to be used for the accurate structure determination of isolated phases (Gemmi & Lanza, 2019), including their refinement (Palatinus, Correa, et al., 2015; Palatinus, Petricek, et al., 2015; Rondeau et al., 2019). It has been successfully used on the Paris CM meteorite for the identification of cronstedtite polytypes (Pignatelli et al., 2018). Multiple scanning transmission electron microscopy (STEM) techniques have proven useful for the study of chondritic materials. Energy-dispersive x-ray spectroscopy (EDS) provides elemental maps. In principle, it could be possible to segment the chemical maps into the different material phases in the samples based on their distinct elemental composition. However, when the grains are much smaller than the typical sample thickness (as in this work), the spectra correspond to mixtures of the different phases in the sample and, therefore, the elemental maps cannot be easily segmented. EDS is often used in combination with other STEM methods, such as bright-field (BF) and high-angle annular dark-field (HAADF) imaging. HAADF has the advantage over HRTEM that the contrast is roughly proportional to the mass × thickness of the sample, easing image interpretation. However, electron-induced beam damage usually precludes atomic resolution HAADF imaging of beam-sensitive materials such as phyllosilicates.

Here, we use four-dimensional scanning transmission electron microscopy (4D-STEM) for the analysis of Ryugu samples. In 4D-STEM, a two-dimensional diffraction pattern is acquired at each point on a two-dimensional grid over the sample, resulting in a four-dimensional data set. There exist multiple 4D-STEM imaging techniques (Ophus, 2019) such as virtual dark-field (VDF) imaging, phase mapping, and orientation mapping. In VDF imaging (see Figure 1b,c), images are obtained by integrating through numerical apertures any desired combination of regions of the reciprocal space (Gammer et al., 2015). In phase mapping, by leveraging the unique electron diffraction signatures exhibited by different mineralogical

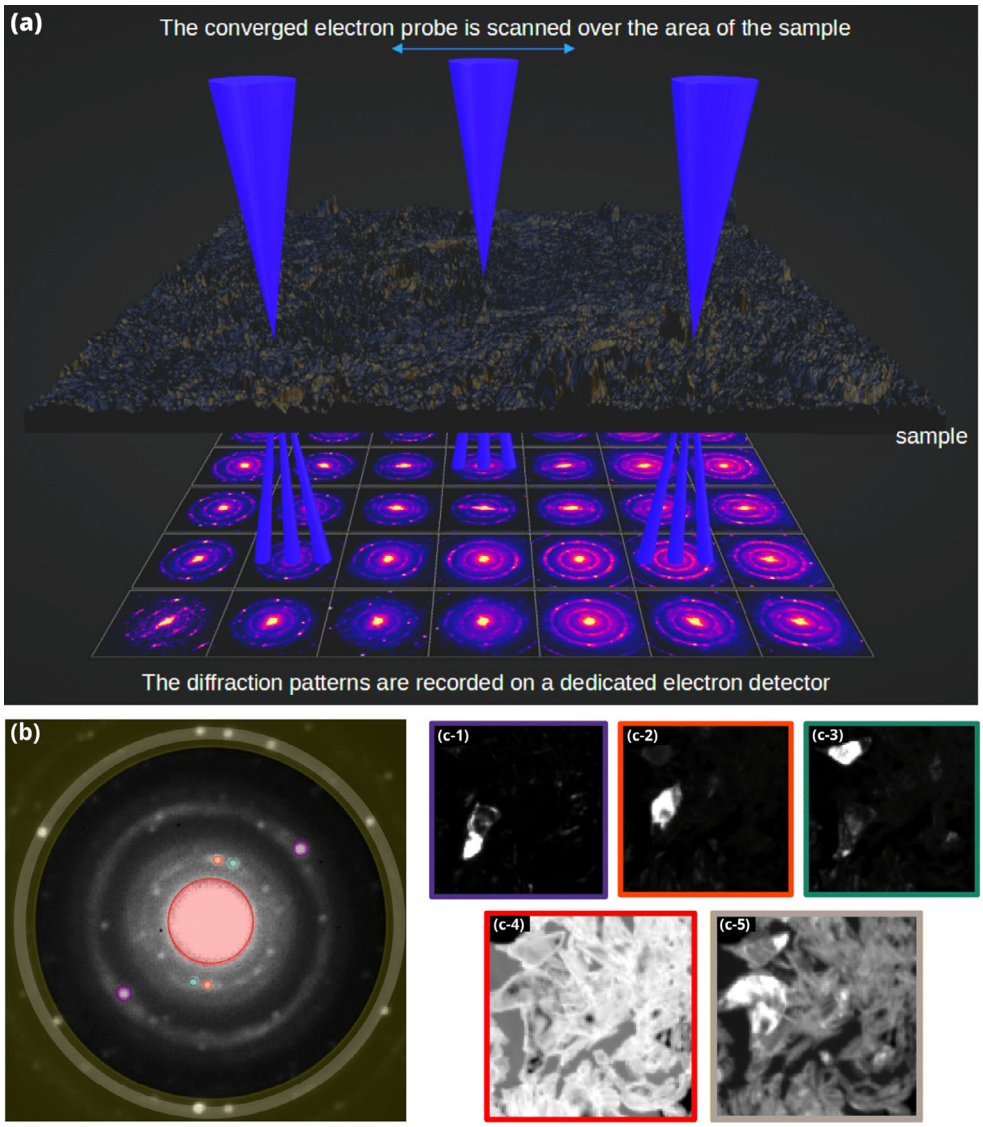

FIGURE 1. (a) Schematic of a typical 4D-STEM experiment. The cones in blue represent the STEM probe being rastered over the sample area. Each diffraction pattern in the figure is an average of 9 × 9 experimental diffraction patterns recorded on a Medipix3 pixelated detector. (b) A 4D-STEM variance diffraction pattern reconstructed from a terrestrial serpentine sample. Overlayed circles are numerical apertures used to reconstruct virtual images shown in the color-coded corresponding figures (c1–c5). We can select any regions of the reciprocal space to reconstruct virtual dark field (VDF) images as shown in (c1–c3). A virtual bright-field (VBF) image is reconstructed by integrating the subset of pixels corresponding to the location of the direct electron beam as emphasized by the red circle in (b). The VBF image is plotted in (c4). An annular virtual dark field is reconstructed by integrating the subset of pixels in the reciprocal space corresponding to a given interplanar spacing for example as shown in (c5). Note that we can also reconstruct virtual dark field images from arbitrary shapes as the yellow shape in (b) which corresponds to an arbitrary VDF reconstruction (not shown here).

phases, their distribution can be mapped through data analysis of the 4D data set (Ophus, 2019; Ophus et al., 2022). Similarly, orientation mapping utilizes electron diffraction information to determine the crystallographic orientation of the phases in a sample (Ophus et al., 2022).

Some chondritic samples consist of phyllosilicates and regions of organic matter that can be easily damaged under electron irradiation (Le Guillou et al., 2013; Li & Egerton, 2003), which imposes a limitation on the achievable spatial resolution in electron microscopy studies in general, and in 4D-STEM in particular. Hybrid-pixel direct electron detectors (DED), thanks to their speed, large dynamic range, and close-to-ideal detective quantum efficiency (DQE), enable the analysis of beam-sensitive materials at higher resolution than possible with standard detectors (Bustillo et al., 2021; Tate et al., 2016). Indeed,

hybrid-pixel DEDs enable scanning electron diffraction (SED) experiments with shorter dwell times per pixel for the same signal quality, hence reducing the electron dose required for a given experiment (Bustillo et al., 2021). Examples of 4D-STEM DEDs applications include structural characterization (Béché et al., 2009; Ophus, 2019; Ophus et al., 2022), high-resolution (HR-) STEM imaging (Li et al., 2022; Pennycook et al., 2019; Yang et al., 2016, 2017), and short- and medium-range order measurements in glassy materials (Ehrhardt et al., 2021; Im et al., 2018). As a result, pixelated detectors based on direct electron detection technology are becoming universal detectors for STEM imaging (Krajnak et al., 2016; Paterson et al., 2020).

In this work, by utilizing 4D-STEM and a Medipix3 hybrid-pixel DED over two samples areas of Ryugu, we were able to identify various mineral phases, including an Ni-bearing variety of pyrrhotite, and we identify the serpentine polymorph as lizardite, which provides valuable insight into the aqueous alteration history of Ryugu. Furthermore, our statistical analysis of smectite d-spacings at the nanometer scale offers new evidence for the potential presence of organic matter within the interlayers of smectite. These findings demonstrate the power of our 4D-STEM-based approach in unraveling the complex mineralogical and chemical composition of extraterrestrial samples.

MATERIALS AND METHODS

Sample Preparation and Data Acquisition

The Hayabusa2 spacecraft retrieved a number of Ryugu grains after two touchdowns in the A and C chambers (Tachibana et al., 2022). The fragment used in this study comes from chamber A of the first touchdown site. The sample studied is A0104-00600303 and was prepared by focused ion beam (FIB) technique at Kyoto University (Helios NanoLab 3G, ThermoFisher Scientific). Two different areas of one FIB section, of thickness $\sim$100 nm were examined in this work using STEM-HAADF, STEM-EDS, and 4D-STEM. Analyses were conducted on a ThermoFisher Titan Themis 300 S/TEM operating at 200 kV at the microscopy platform of the University of Lille. The Titan Themis is equipped with a high brightness Schottky field emission gun (FEG), a monochromator, and a probe corrector. The STEM-EDX mapping of the investigated areas was performed on a ThermoFisher super-X windowless 4 quadrants silicon drift detection (SDD). 4D-STEM data sets (Figure 1a) were acquired on a Medipix3 Merlin hybrid-pixel DED (Plackett et al., 2013) installed in a Gatan post-column energy filter (GIF) (Quantum ERS/966), enabling energy-filtered 4D-STEM. Three data sets denoted R1U, R1F, R2U were acquired from two different regions. The first region was analyzed twice; first without energy filtering (R1U) and then again with energy filtering (R1F). The second area was analyzed once without energy filtering (R2U). In all acquisitions, a convergent electron probe was rastered on a 128 × 128 grid covering a $\sim$1 × 1 μm area. The convergence semi-angle was 0.1 mrad. The full-width half-maximum (FWHM) of the probe profile was $\sim$7 nm. The dwell time per pixel was 3.5 ms for both acquisitions on the first area and 20 ms for the second area. No beam damage was observed after the 4D-STEM acquisitions.

Analysis of 4D-STEM Data

The acquired data were analyzed using the open-source Python packages py4DSTEM (Savitzky et al., 2021) and HyperSpy (De la Peña et al., 2022). The analysis involves a number of common preprocessing steps followed by radial analysis and specific processing procedures for the different 4D-STEM imaging techniques.

Preprocessing

All the 4D-STEM data were preprocessed prior to further investigation as follows:

- *Dead pixel correction*: Dead pixels are malfunctioning pixels that do not respond to incoming electron signals or do not produce a measurable output. These pixels were corrected through linear interpolation with neighboring pixels.
- *Diffraction stack alignment*: The method utilized is described in detail in Savitzky et al. (2021). The data were cropped to only retain the direct beam. The second diffraction pattern in the stack was cross-correlated with the first one to find its relative offset, and then the second pattern was shifted to align with the first one. The third pattern was then aligned with the second, and so on until all the diffraction patterns in the stack were properly aligned.
- *Vacuum probe and probe kernel*: The objective is to extract the shape of the electron probe for pattern matching. First, pixels corresponding to vacuum or very thin areas in the sample are identified, and the corresponding diffraction patterns are averaged to generate a two-dimensional image of the unscattered electron probe in diffraction space, which is referred to as the vacuum probe. A kernel for cross-correlative template matching is generated in two steps: The vacuum probe is centered and shifted to the origin to remove any offset in the measurements. Then, a wider Gaussian is subtracted from the probe, resulting in a negative intensity region around the probe to ensure

that the total integrated intensity of the kernel is zero (for more details, see Savitzky et al. (2021)).

Processing

- *Bragg spot registration*: In this step, diffraction spots are found by calculating the cross-correlation of the probe kernel generated in the preprocessing step with each individual diffraction pattern in the 4D-STEM stack, and then locating the correlation maxima (for details, see Savitzky et al. (2021)). This results in a list of Bragg spots detected, where each spot is defined by the coordinates of the pixel containing the diffraction pattern from which they originate (a unique pair (x, y)), the coordinates of the different spots detected in the reciprocal space (q_x, q_y) and the intensity of each of these spots.
- *Mineralogical phase identification*: Several virtual diffraction patterns can be useful for identifying the mineralogical phases present in the surveyed area. An average diffraction pattern can be generated by summing up all the diffraction patterns in the 4D data stack, which can be regarded as equivalent to a selected area electron diffraction (SAED) pattern. This can then be azimuthally integrated to obtain an average radial profile over the surveyed area. However, the Bragg spots from minor phases may be obscured in the average diffraction pattern. Therefore, we mainly rely on the variance diffraction pattern (vDP) and the Bragg vector map (BVM) to obtain an overview of the mineralogy. The vDP is the variance intensity of every diffraction pixel across the entire data set. The BVM is a reconstructed pattern obtained by merging all the diffraction peaks detected via the peak detection processing step previously described from every diffraction pattern in the 4D stack in a single image (for more details, see Savitzky et al. (2021)). We can then azimuthally average the BVM pattern and use the resulting 1D profile for x-ray diffraction-like mineral phase identification.
- *Template matching*: Template matching involves comparing experimentally obtained diffraction patterns with simulated diffraction patterns generated from crystallographic information files (CIF) after the Bragg peaks finding procedure. The resulting correlation values are calculated to identify the crystal structure or orientation. A high correlation value indicates a good match, but the specific threshold for a "good match" value varies depending on the material and quality of data. For more details on the template matching procedure and the underlying mathematical framework, we refer readers to Ophus et al. (2022).
- *Virtual imaging and phase mapping*: In virtual dark field imaging, specific pairs of diffraction spots from the reciprocal space are used to create virtual images that highlight specific regions of the sample. Integration is performed over the intensities of the diffraction spots that correspond to these regions. For instance, selecting diffraction spots corresponding to a particular crystal orientation produces a VDF image that highlights that orientation (Figure 1b,c1–c3). Similarly, the direct beam in the diffraction pattern is selected to produce a virtual bright-field (VBF) image (Figure 1b,c4). Furthermore, selecting an annular region in the diffraction pattern generates an annular VDF image that highlights the sample regions that diffracted within that specific annulus (Figure 1b,c5). By using these different types of virtual imaging techniques, different regions of the sample can be mapped out. In this particular study, a comprehensive map of the mineralogical features within the sample is generated by selecting and integrating over sets of diffraction peaks detected in the areas under examination, which can be correlated to their chemistry. Valuable insights into the sample's composition and microstructure can be obtained as a result.

RESULTS

STEM-HAADF images from areas of the examined FIB section show typical heterogeneous mixtures of fine-grained matrix components (Figure 2). The dominant component is the phyllosilicate matrix (PSM). It constitutes a groundmass where other minerals such as sulfides are present in various proportions.

The image in Figure 3a is a VBF reconstruction from the 4D-STEM data set (R1F), which corresponds to the STEM-HAADF image in Figure 2a. An average diffraction pattern over the whole surveyed area is shown in Figure 3b alongside a vDP in Figure 3c and a BVM in Figure 3d over the same area. The vDP and the BVM virtual diffraction patterns better emphasize weakly diffracting phases and/or diffraction spots from minor phases which can be obscured in the average diffraction pattern. Consequently, these maps provide additional information about the phases that are present and can be used to investigate deviations from the dominant phase. These differences can be better emphasized by azimuthally integrating these virtual patterns as shown in Figure 3e,f.

General Description of Ryugu's Mineralogy

Structural identification of different mineralogical phases present in Ryugu matrix can be obtained by analyzing the BVM-based radial profile of Figure 3e and correlating with VDF imaging to identify each diffraction peak in the profile.

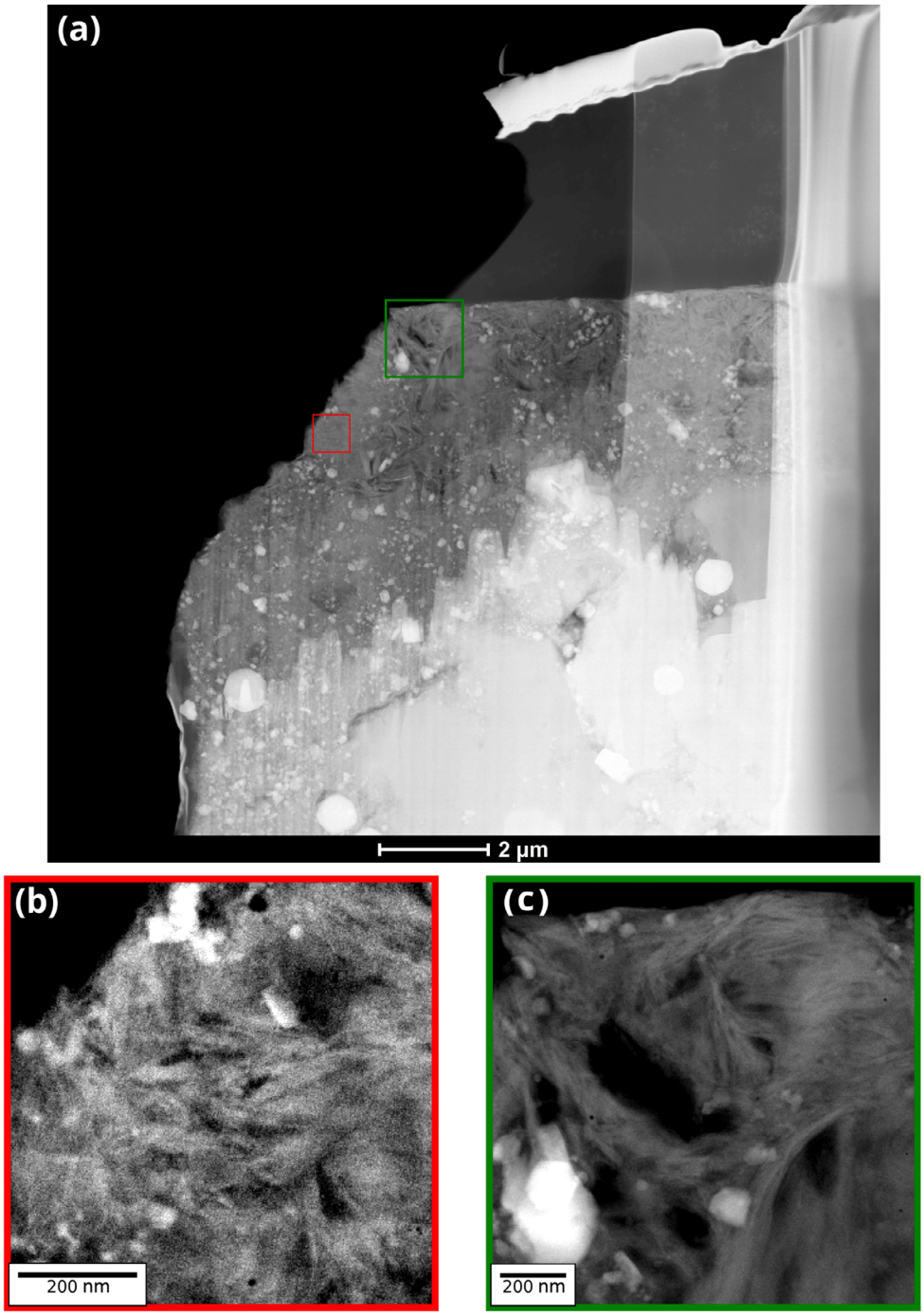

FIGURE 2. (a) A low magnification high-angle annular dark field (HAADF) image of the sample A0104-00600303, with color-coded boxes overlayed to indicate the specific areas that were further examined by EDX and 4D-STEM and which the corresponding high magnification HAADF are shown in (b, c). Both areas examined are magnetite and carbonates free and the brighter regions correspond to Fe-bearing sulfides.

Sulfides

Iron and iron–nickel sulfides have characteristic peaks located at ~0.55, ~0.29, ~0.2, ~0.179, and ~0.169 nm (see Viennet et al., 2023). Taking all these peaks into account, a combined VDF image of sulfides along with a corresponding EDX map over the same area are shown in Figure 4a,b, respectively. A clear

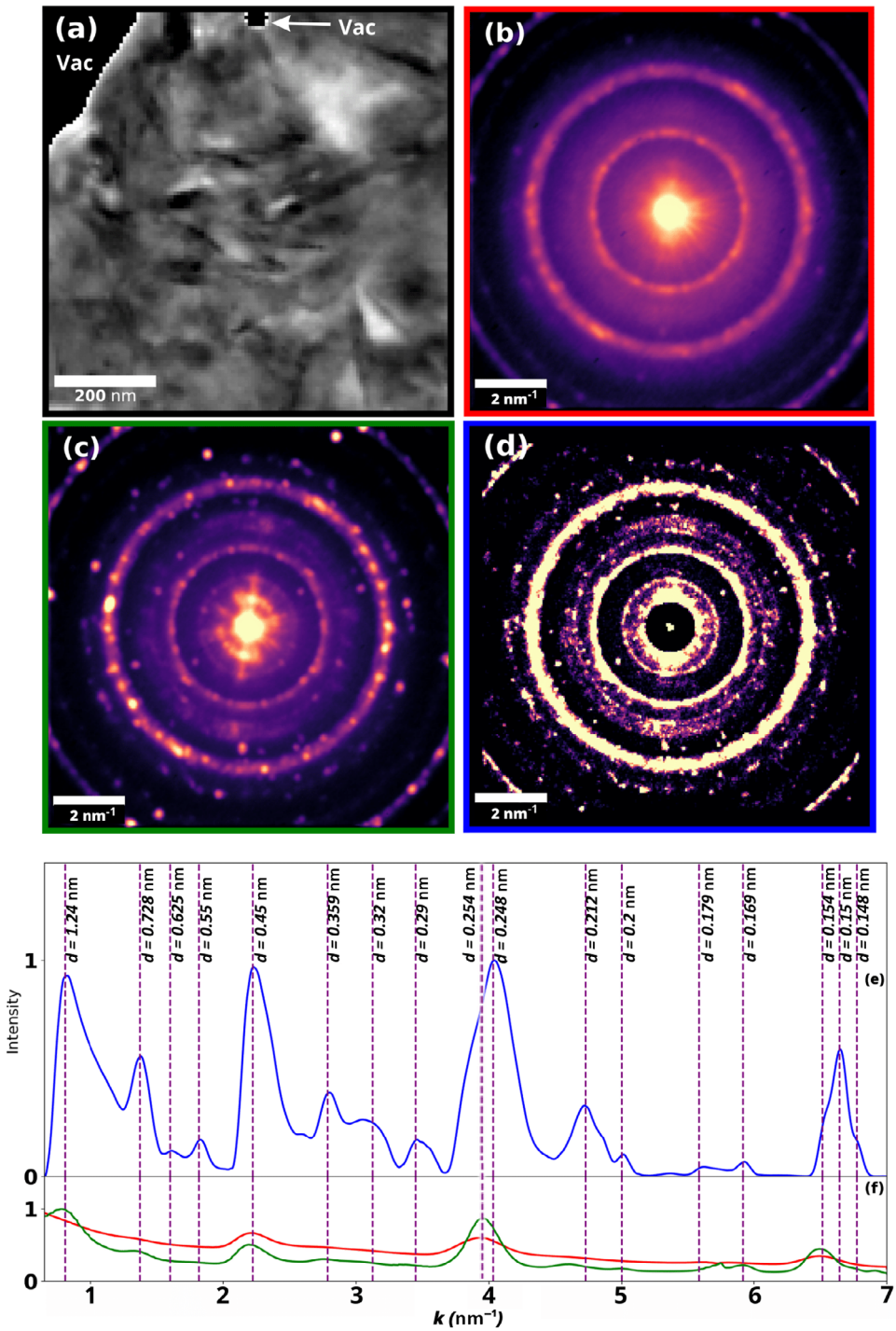

FIGURE 3. (a) Virtual bright-field (VBF) image of the area corresponding to the HAADF image in Figure 2a. Figures (b–d) correspond to the mean diffraction pattern, the variance diffraction pattern, and the Bragg vector map of the whole 4D-STEM data set (R1F), respectively. Corresponding 1D radial profiles, obtained by azimuthally averaging diffraction patterns (b–d) are shown in (e, f) color coded to match the corresponding diffraction patterns. While the BVM-based radial profile show characteristic peaks of all the minerals present in the area that was investigated, the average radial profile captures mainly the *hk0* reflections of phyllosilicates while the variance radial profile captures the 001 reflections as well as the *hk0* reflections of phyllosilicates. The radial profile obtained by integrating the Bragg vector map can be used to describe the mineralogy of Ryugu asteroid.

consistency between the two image reconstructions is observed. Figure 4c–e are diffraction patterns obtained from the 4D-STEM data over the areas that are highlighted in Figure 4a. Template matching (described in more details in Ophus et al. (2022)) of pyrrhotite and pentlandite diffraction pattern libraries (calculated with, respectively, space groups $P3_121$ (Nakano et al., 1979) and *Fm*-3*m* (Rajamani & Prewitt, 1975)) with the sample diffraction patterns were performed using the automated crystal orientation mapping (ACOM) module of py4DSTEM (Ophus et al., 2022). These patterns were properly indexed as pyrrhotite as shown in Figure 4f,g, while pentlandite did not match these diffraction patterns at all. This suggests that Ryugu may contain Ni-bearing pyrrhotite which is consistent with the findings of Harisson et al. (2022), Ito et al. (2022), and Nakamura et al. (2023). The gray areas of Figure 4a have corresponding diffraction patterns that lacked enough Bragg spots to be indexed, and hence, no structure information was retrieved to complement the chemical information. The interested reader can consult in-depth investigations on the formation of Ni-bearing pyrrhotite and pentlandite in CI-chondrites described in Berger et al. (2016) and Schrader et al. (2021).

Serpentine and Smectite

The radial profile in Figure 3e corresponding to the mean diffraction pattern in Figure 3b displays three relatively broad diffraction peaks at ~0.45, ~0.254, and ~0.154 nm. Following Brindley and Brown (1980), these peaks have been attributed to reflection on (2,11,0), (13,20,0), and (6,33,0) planes of phyllosilicates. This suggests that most of the pixels in the examined area are mainly made up of a mixture of fine-grained smectite and Mg-rich serpentine (King et al., 2015; Tomeoka & Buseck, 1988).

In agreement with Viennet et al. (2023), the peaks located at ~0.728 and ~0.359 nm in Figure 3e correspond to the serpentine 001 and 002 reflections, respectively, while the peak located at ~0.212 nm corresponds to the 112 reflection of serpentine. The intense peak around ~1.24 nm corresponds to the 001 reflection of smectite. A small contribution can also be seen from the 002 reflection of smectite at ~0.625 nm and a relatively broad peak located at ~0.32 nm is attributed to the 004 reflection of smectite.

In the area shown in Figure 5a, a virtual dark field map of smectite and serpentine distribution in the phyllosilicate matrix was obtained, as shown in Figure 5b. This was accomplished by integrating over the smectite and serpentine 001 diffraction rings and over the phyllosilicate reflection at ~0.45 nm. The boundaries of the diffraction rings used for the integration are determined by the width of the corresponding peaks in the 1D radial profiles. On this virtual dark field, serpentine- and smectite-rich areas are, respectively, colored in green and red whereas mixed areas are colored in blue. An element map obtained by STEM-EDS showing Si/Mg ratio is shown in Figure 5c. In favorable cases, serpentine and smectite can be distinguished through STEM-EDS analysis. Without taking into account possible Al substitutions, Mg-rich serpentine exhibits a Mg/Si ratio of ~1.5, while smectite, possessing a permanent charge of 0.4, has an Mg/Si ratio of ~0.83. However, the mixing scale between both phases is often smaller than our pixel size in the EDX maps and, therefore, only the larger grains can be reliably identified in this way. Comparison of Figure 5b,c indicates that smectite-rich areas oriented with (001) planes edge-on are correlated with Si-rich areas in the corresponding elements map (both in red). Nevertheless, serpentine (001) area as well as smectite-serpentine rich areas (green and blue, respectively) are both associated with Mg-rich areas (blue on the EDX map). It shows that 4D-STEM identifies serpentine and smectite grains at a finer scale than EDX when they are properly oriented with basal planes edge-on.

Serpentine in Ryugu

Serpentine are 1:1 tri-octahedral phyllosilicates. The three most common polymorphs of serpentine are lizardite, antigorite, and chrysotile which are all Mg-dominant. The ideal chemical formula of serpentines is $Mg_3Si_2O_5(OH)_4$. They only differ in terms of how their fundamental coordinating polyhedra are oriented one to each other. These form flat layers in the case of lizardite, wavy layers in antigorite, and curled layers in chrysotile (Andreani et al., 2008; Mellini, 2013; Vance & Melwani, 2020). Chrysotile is common in CM chondrites (Barber, 1981; MacKinnon, 1980) but rare in CI chondrites (Tomeoka & Buseck, 1988) and is easily recognized by high-resolution TEM because of its apparent tubular structure (Yada, 1971). No previous investigations of Ryugu asteroid samples have indicated the presence of chrysotile; neither has the current study.

In order to identify the polymorph that can be most representative of serpentine in the PSM of Ryugu among lizardite and antigorite, a set of pixels (~20 pixels) of serpentine that are close to Bragg conditions were chosen from the second area (R2U) examined in this study (Figure 2b). This was accomplished by template matching of experimental diffraction patterns with simulated patterns of lizardite and antigorite using libraries from Mellini et al. (2010) for lizardite and Uehara (1998) for antigorite. We used the ACOM module of py4DSTEM to compare the experimental diffraction patterns in the 4D-

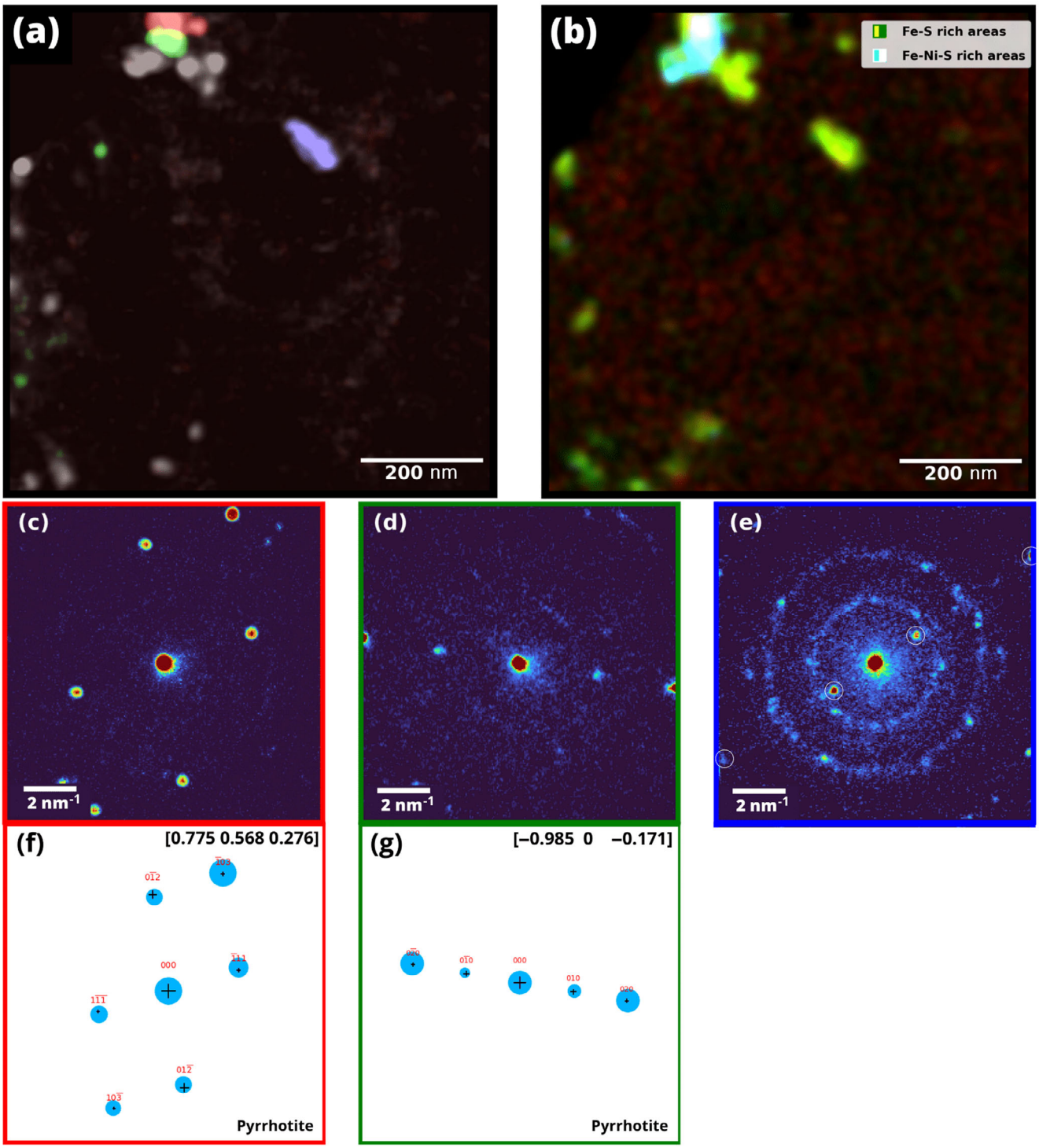

FIGURE 4. (a) Combined virtual dark field image made by 4D-STEM (b) showing Ni-free and Ni-bearing sulfides in the examined area and (b) corresponding STEM-EDS maps. (c–e) Color-coded diffraction patterns corresponding to the different areas of equivalent color shown in (a). Gray areas in (a) correspond to sulfides that could not be indexed due to insufficient diffraction spots in the corresponding DPs. White circles in (e) indicate diffraction spots relevant to the corresponding iron-rich sulfide in (a). Indexing diffraction patterns of (c, d) shows that both the Ni-free and Ni-bearing sulfides are pyrrhotite (f, g).

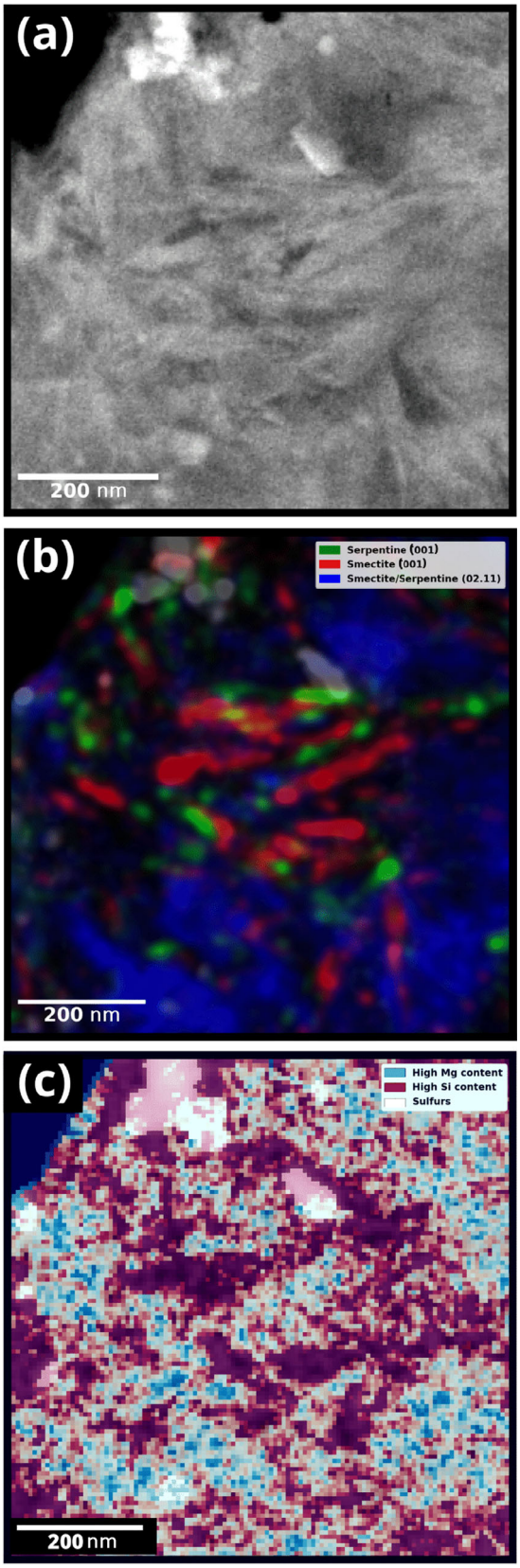

FIGURE 5. (a) STEM-HAADF image of the surveyed area (same as Figure 2a). (b) A corresponding combined virtual dark field image made by 4D-STEM showing smectite and serpentine distribution in the matrix along with (c) energy-dispersive x-ray spectroscopy (EDS) map made by scanning transmission electron microscopy (STEM) of Mg/Si ratio over the same area. Sulfides in (b) are imaged in light gray for a better localization of the different features observed in (a) and (c).

stack to the template patterns and retained only the pixels that showed correlation values >0.5 for both cases. We selected this threshold value because we found it to be the minimum value that excluded diffraction patterns for which the corresponding simulated patterns were obviously different from the measured ones. Afterward, the diffraction patterns of these pixels were summed and then azimuthally integrated to get the radial profile in Figure 6b. For clarity, diffraction patterns corresponding to only three different pixels are shown in Figure 6c1–c3. From the template matching results, the correlation value between Ryugu's serpentine diffraction patterns and lizardite simulated diffraction patterns was consistently higher than that of antigorite as shown in Figure 6. This was observed in all the pixels that corresponded to serpentine close to the Bragg conditions. Furthermore, the simulated diffraction patterns of antigorite in Figure 6 suggest that certain spots in the corresponding experimental patterns should exhibit a perpendicular streaking, which is not observed here. Perpendicular streaking is also commonly observed in SAED patterns of both antigorite and chrysotile (Zvyagin, 1967). This supports the interpretation that serpentine in the PSM of Ryugu is most likely present in the form of lizardite.

Smectite in Ryugu

Smectite minerals are a type of clay mineral that belongs to the phyllosilicate family and have a T-O-T structure. Isomorphic substitutions in variable amounts by lower charge cations in tetrahedral and/or octahedral sheets induce negatively charged 2:1 layers, the so-called "permanent charge." This permanent charge is in turn compensated by hydrated exchangeable cations in the interlayer space that are responsible for the hydration properties leading to the expansion of the layer-to-layer distance reflected by the position of the (001) reflection (Ferrage, 2016). The layer-to-layer distance depends on the hydration state. Indeed, the tri-hydrated state of smectite, characterized by the presence of three water molecules between the layers, leads to a layer-to-layer distance of up to $\sim$1.9 nm, while a dehydrated state reduces the distance to $\sim$0.96 nm (Colten-Bradley, 1987;

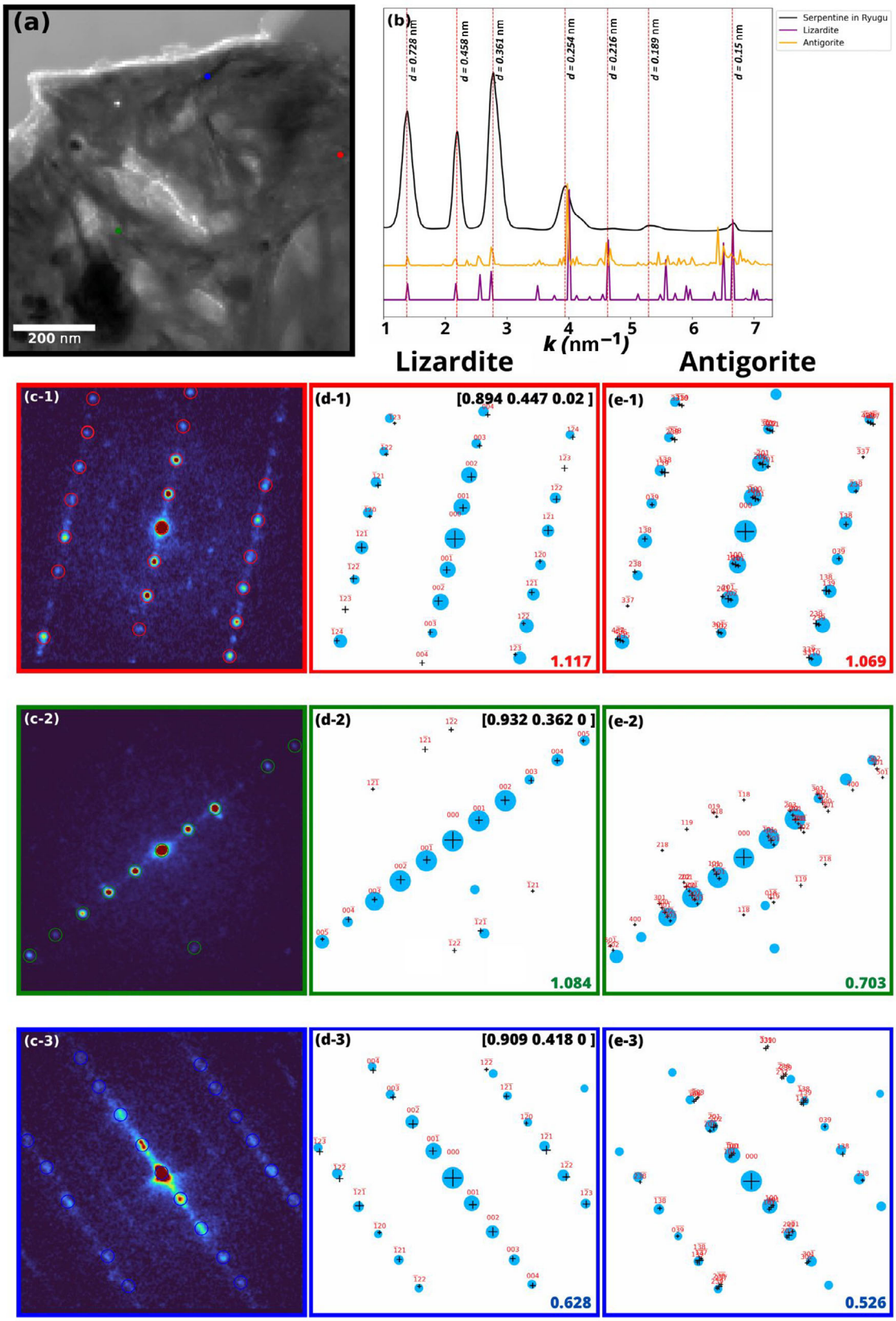

FIGURE 6. (a) A reconstructed VBF image of the area that was examined in 4D-STEM along with a corresponding average radial profile reconstructed from the diffraction patterns of the 4D data stack. The homogeneous light gray region in top is vacuum. (b) 1-D histogram of scattering vectors from oriented serpentine (black) and simulated electron diffraction profiles of lizardite (purple) and antigorite (yellow) with serpentine's detected inverse plane spacings overlaid. (c1–c3) are diffraction patterns from the three separate color-coded areas of serpentine in (a) along with (d1–d3) lizardite matches and (e1–e3) antigorite matches of the respective diffraction patterns. Lizardite's and antigorite's correlation scores are shown in the bottom right of their respective matches showing that the correlation score for lizardite is higher than that of antigorite. Best-fit zone axes of lizardite are shown in the top right of their respective matches.

Ferrage, 2016; Moyano et al., 2012; Sayers & den Boer, 2016). The radial profiles in Figure 3 for Ryugu samples indicate that smectites have a mean d-spacing of ~1.24 nm. Using 4D-STEM, it is possible to map the variation in the interlayer spacing of smectite by determining the d_{001} spacing at each scan position. This was accomplished on the filtered data used in this study (R1F) by first cropping each diffraction pattern to only retain a region of the reciprocal space up to a reciprocal space radius of 1.1 nm^{-1}. This selection restricts our analysis to the 001 reflection areas of smectite, corresponding to a minimum observable real space distance of ~0.9 nm. Afterward, the peak finding procedure described in the previous section is used over this newly formed data set to extract the positions of each pair of diffraction spots and measuring their spacing, and hence, the d_{001} of smectite. A histogram of the different smectite d-spacings identified by this procedure in the area examined by 4D-STEM is shown in Figure 7. It suggests that d-spacings are ranging from ~1 to ~2 nm. Most d-spacings lie between ~1 and ~1.4 nm with a mean value that is around ~1.24 nm as previously emphasized by the radial profiles of Figure 3e.

Figure 8a shows a VDF image reconstructed using the (001) reflection of smectite. At each smectite pixel in the surveyed area, we have a value for the interlayer spacing, which results in a map of the interlayer spacing of smectite that is shown in Figure 8b. The map displays a random distribution of d-spacing values without any discernible patterns or trends. Some representative diffraction patterns selected from a set of pixels in the smectite-rich area are displayed in Figure 8c1–c6.

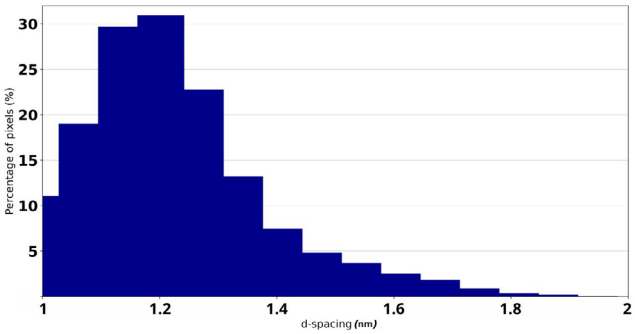

FIGURE 7. A histogram of the variability of d-spacings in the examined area of Ryugu showing, as a percentage, the frequency of smectite pixels in the map that correspond to a given d-spacing. Most d-spacings lie between ~1.1 and ~1.4 nm while some other pixels (<5%) display larger interlayer spacing values.

DISCUSSION

The Ryugu samples studied here are important to understanding the mineralogy and crystallization history of the asteroid (e.g., Dobrică et al., 2023; Ito et al., 2022; Nakamura et al., 2023; Yada et al., 2022). The identification and characterization of minerals in these samples are crucial for unraveling the formation processes and environmental conditions that shaped Ryugu. To achieve comprehensive mineralogical analysis, advanced techniques capable of high-resolution imaging and diffraction are required. In this regard, the emergence of 4D-STEM using direct electron detection technology has opened up new possibilities for investigating complex and beam-sensitive samples (e.g., Bustillo et al., 2021; Li et al., 2022; Ophus, 2019; Ophus et al., 2022; Savitzky et al., 2021). One of the most significant benefits of 4D-STEM over SAED is its ability to offer both high spatial resolution and representative sample measurements over several μm^2. Phase and orientation mapping of beam-sensitive materials is now feasible, providing important information on the presence or absence of orientation relationships and hence the crystallization history of the sample.

It is noteworthy that the 4D-STEM data set we used for depicting the mineralogy of Ryugu (data set R1F) is acquired with zero-loss energy filtering. To illustrate the effect of filtering, we show in Figure 9a,b two variance diffraction patterns that were reconstructed from two separate 4D-STEM data sets taken from the same area (HAADF image Figure 2a). The first data set was acquired without filtering (R1U), while the second was acquired with filtering (R1F). The energy filtering removes the inelastic scattering from the diffraction patterns (mainly plasmon scattering collection at low angles (Yi & Voyles, 2011)), which can cause broadening of the diffraction spots and decrease the contrast in the

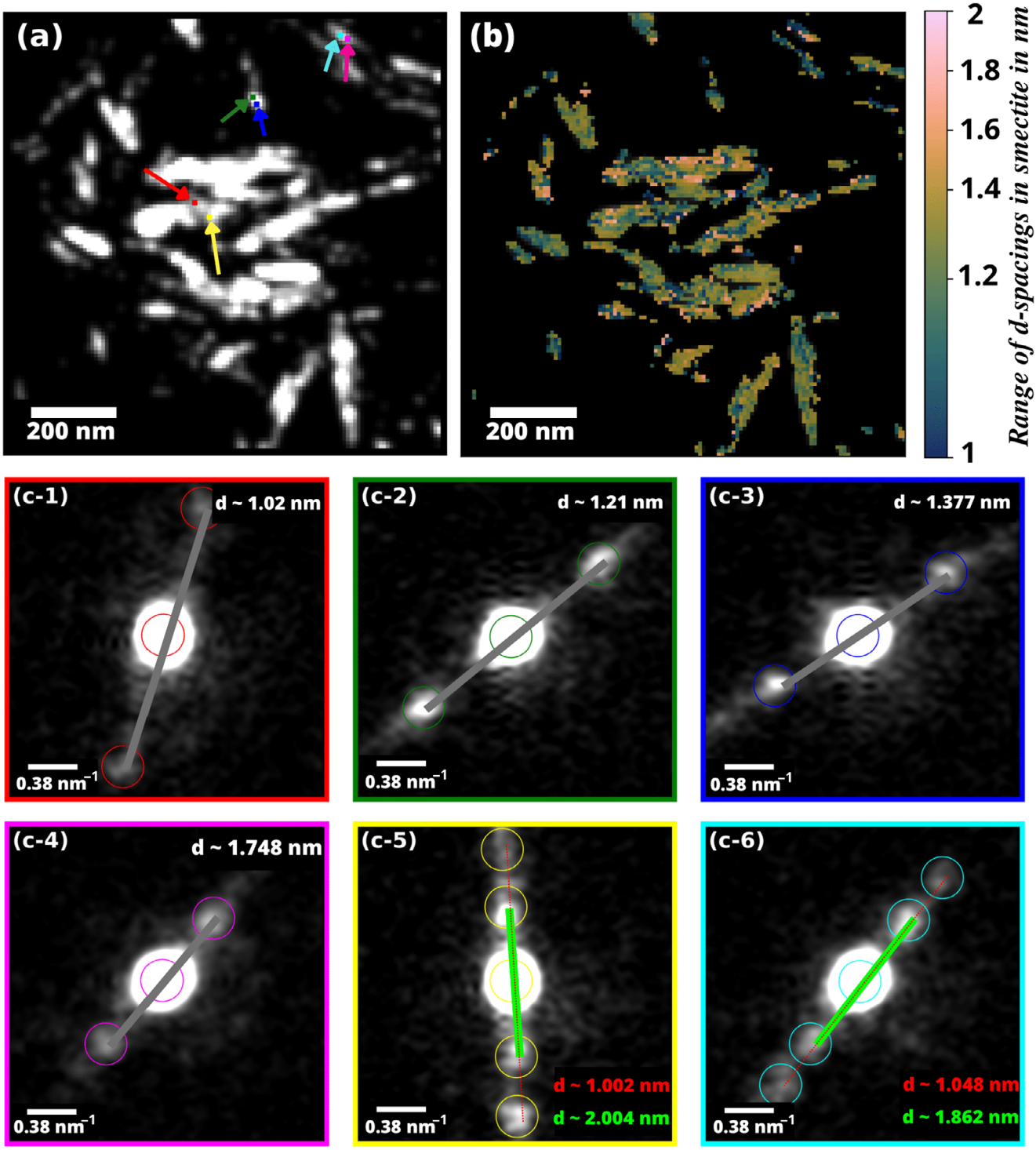

FIGURE 8. (a) VDF image of smectite-rich area in Ryugu reconstructed from the 001 reflection. Colored arrows indicate pixels from which a set of diffraction patterns are taken as a showcase. (b) A map of the distribution of the interlayer spacing in smectite over the same area shown in (a). (c1–c6) are diffraction patterns taken from the pixels color-coded in (a). A variety of d-spacings ranging from ~1 to ~2 nm were observed.

diffraction pattern (Figure 9a). This results in a clearer diffraction pattern with sharper spots and reduced background. Figure 9c depicts the one-dimensional azimuthally averaged profiles of the two variance diffraction patterns, which are color-coded for clarity. Notice that the smectite and serpentine reflections are

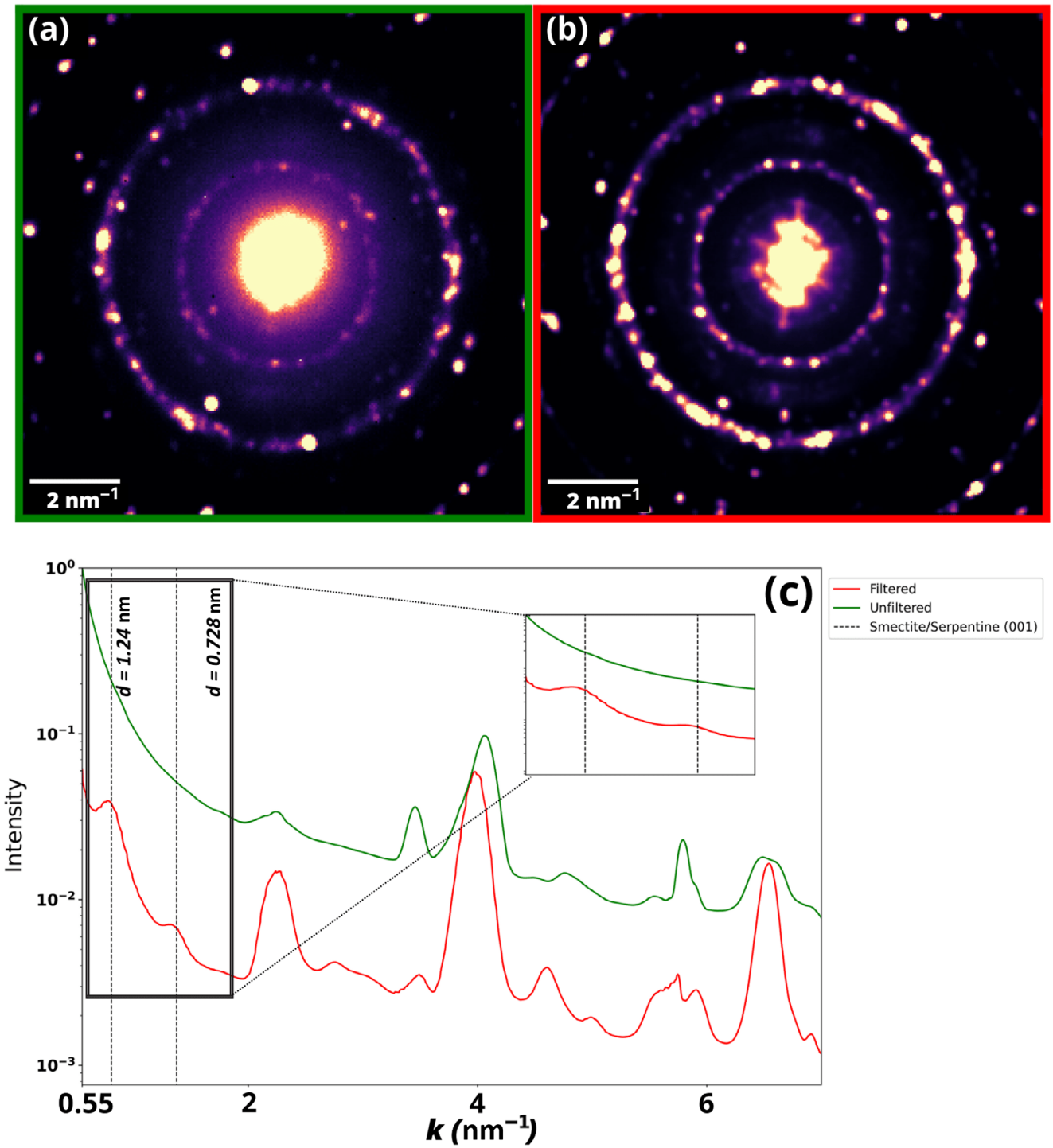

FIGURE 9. The effect of zero-loss energy filtering. A variance diffraction pattern over the area under investigation (a) without filtering and (b) with filtering. The corresponding azimuthally averaged one-dimensional profiles are shown in (c). We can clearly see that the intensity near the zero beam is higher without energy filtering which makes the diffraction signal of smectite and the 001 of serpentine near the direct beam very weak, hence, cannot be emphasized without energy filtering. We should note here than the unfiltered 4D-STEM data set (R1U) was acquired prior to the filtered one (R1F).

hardly discernible in the unfiltered radial profile with a dwell time of 3.5 ms, but clearly visible in the radial profile obtained with energy filtering. In data set (R2U), we increase the dwell time to 20 ms to improve the signal-to-noise (SNR) ratio to enable serpentine phase identification. While this enabled the detection of the 001

reflection of serpentine, it was not possible to detect the 001 reflection of smectite. As previously described, low-angle scattering features, such as smectite 001 d-spacing, can be resolved more effectively in electron diffraction when using zero-loss energy filtering. Therefore, if energy filtering had been employed to acquire the data set, it would likely have been possible to resolve the 001 reflection of smectite.

Using 4D-STEM, we were able to accurately identify and map the different minerals present in Ryugu. The regions analyzed in this study did not include magnetite and carbonates, also present in Ryugu (Dobrică et al., 2023; Ito et al., 2022; Nakamura et al., 2023; Yada et al., 2022), as we focused on phases of smaller grain size. Instead, our main focus was on the phyllosilicates.

Several studies tried to address the identification of the serpentine polymorph in the phyllosilicate matrices of chondrites. For instance, Takir et al. (2013) used IR analysis on the Ivuna CI-chondrites and detected the presence of both lizardite and chrysotile, but was unable to differentiate between them. Osawa et al. (2005) also reported, from IR spectra analysis, the signature of lizardite in Ivuna CI-chondrite, and that of chrysotile in CH and CB chondrites. TEM studies, however, have generally been able to distinguish serpentine polymorph based on the appearance of basal lattice fringes. For instance, chrysotile has been identified in CM chondrites by HRTEM studies based on its tubular structure (Tomeoka & Buseck, 1985). Additionally, the presence of polyhedral serpentine in Murchison, Mighei, and Cold Bokkeveld CM chondrites was reported by Zega et al. (2006) using TEM imaging. They also proposed a possible pathway for its formation through alteration and oxidation of cronstedtite on the parent body. Determining the main serpentine polymorph in the matrix may provide clues about the conditions and processes that occurred during the formation and alteration of the parent body.

In this study, and by means of template matching, over a selection of diffraction patterns close to exact Bragg conditions taken from serpentine areas, we have identified the serpentine polymorph present in Ryugu to be lizardite. Investigating the conditions under which lizardite forms and the mechanisms that drive its formation will provide valuable information about the history and evolution of Ryugu. Serpentine minerals are known to form through a process called serpentinization, which involves the hydration of minerals that contain iron or magnesium, such as olivine (Bailey, 1991). When olivine interacts with water, the crystal structure of the mineral breaks down, leading to the formation of lizardite with possibly magnetite and brucite (Bailey, 1991). A work conducted by Wenner and Taylor (1971) measured ^{18}O-fractionations between coexisting serpentine and magnetite to give approximate temperatures of serpentinization of ultramafic rocks. They found that, at fluid pressures up to ~4 kbar, different chrysotile–lizardite mixtures occur at temperatures ranging from 85 to 185°C, while antigorite is stable at even higher temperatures. This is in agreement with other studies by O'Hanley et al. (1989) and O'Hanley and Wicks (1995), which investigated the stability of serpentine polymorphs under different conditions. In these studies, they reported that, under fluid pressures up to ~4 kbar, the stability of serpentine polymorphs changed with increasing temperature. Specifically, lizardite was found to be the most stable phase at temperatures below 200°C, but as temperature increased, it was replaced by chrysotile. At even higher temperatures, the most stable serpentine polymorph was observed to be antigorite. A more recent study by Evans (2004) focused on the role of temperature and reported that lizardite is favored at lower temperatures. However, its stability diminishes as the temperature surpasses 290°C, and antigorite–brucite assemblage becomes stable. Schwartz et al. (2013) investigated phase transitions between the different polymorphs of serpentine and observed that below 300°C and 4 kbar, only lizardite is stable, while in the 320–390°C range of temperatures, and for pressures >9 kbar, antigorite progressively replaces lizardite. Since the present study suggests that lizardite is the predominant serpentine polymorph in Ryugu samples, it is likely that aqueous alteration occurred at low temperatures that are favorable for lizardite formation. This is consistent with recent studies of Ryugu grains. Nakamura et al. (2023) concluded, from the low abundance of Mg-chlorite, that aqueous alteration may have occurred at temperatures below 100°C while Yamaguchi et al. (2023) reported that the alteration temperature does not exceed 210°C. Yet, the implications of lizardite formation discussed here might not be directly applicable to Ryugu and CI-chondrites meteorites because the precursor materials for the serpentine are still unknown. Indeed, our study did not find any evidence of amorphous, gel, or glass-like minerals in Ryugu from which a serpentine phase like lizardite could eventually be formed. However, as pointed out by Leroux et al. (this issue) and Nakamura et al. (2023), a part of serpentine could have been formed from anhydrous silicate material such as Mg-rich olivine and pyroxene.

The detection of smectite in Ryugu grains is consistent with previous results on the mineralogy of Ryugu (Ito et al., 2022; Leroux et al., this issue; Nakamura et al., 2023; Noguchi et al., this issue; Yokoyama et al., 2022). As for serpentine, smectite is an aqueous alteration product particularly abundant in CI chondrites (e.g., King et al., 2015; Tomeoka & Buseck, 1988). Considering desorption of interlayer water molecules under vacuum conditions of the TEM, the

expected value for the interlayer space should be around ~1 nm. The 4D-STEM results reported here show that the average d-spacing of smectite in the examined area is ~1.24 nm. Common d-spacing uncertainties are generally <5%, which is far below the ~20% dispersion (FWHM) of the distribution reported in Figure 7. So far, smectite's d-spacing had been inferred locally using HRTEM (Noguchi et al., this issue), and as a bulk value using XRD (Nakamura et al., 2023; Viennet et al., 2023; Yamaguchi et al., 2023). The average d-spacing value here measured is consistent with the study led by Viennet et al. (2023) through XRD experiments at 0% relative humidity. This, together with the high dispersion of the d-spacings distribution, indicates that species other than water could be present within smectites' interlayer space, not volatile enough to be released under vacuum. Indeed, using thermogravimetric analysis, Yokoyama et al. (2022) showed that smectite in Ryugu contain little or no interlayer water. One likely candidate then is organic matter. The presence of organic matter within the interlayer space of smectites would lock the interlayer space of smectites at d-spacings >1 nm under 0% RH or under vacuum. This behavior is long known in 2:1 phyllosilicate as organic intercalation (Lagaly & Beneke, 1991; Lanson et al., 2022). More recently, experiments dedicated to the investigation of the interaction between organics and phyllosilicates in chondritic-like conditions revealed the same behavior (Viennet et al., 2019, 2020, 2021, 2022, 2023). Stroud et al. (this issue) studied Ryugu's organic matter and its relationship to minerals at the micrometer to nanometer scale. Yabuta et al. (2023) investigated the abundant organic matter within the Ryugu grains, composed of aromatic and aliphatic carbons, ketones, and carboxyls. They discussed the interaction between minerals and organics based on the presence of diffuse organic matter, supporting the possibility of organic matter's involvement in the interlayer space of smectites. In our study, the ratios of K/Si, Na/Si, and Ca/Si over smectite-rich areas identified with 4D-STEM VDF imaging were below our detection limits (<0.01, not shown) to be responsible for charge compensation in the interlayers of smectite, indicating that, apart for possible residual water molecules, organic matter could be the main species compensating the permanent charge of smectite layers.

While XRD provides a bulk scale d-spacing value (Viennet et al., 2023), 4D-STEM is a powerful complementary source of information. Indeed, our 4D STEM results indicate a considerable degree of heterogeneity among the smectite d-spacings at a scale of ~80 nm, with values ranging from ~1 to ~2 nm. This heterogeneity can have different interpretations. Distinct organic molecules, with different carbon chain lengths for instance, may be present within the interlayer space (Lanson et al., 2022). Alternatively, it could be possible for the same organic molecules to exhibit different spatial arrangements or configurations. Since the d-spacing heterogeneity cannot be attributed to one specific cause, it is difficult to determine its origin. However, one possible explanation for the observed variability is the influence of local geochemical conditions, which can be related to the nature of organic matter and its interactions within the smectite layers. Furthermore, if such heterogeneity is related to variations in the crystal chemistry of smectite layers, such differences could be attributed to local variations in geochemical conditions and/or smectite precursors. The d-spacing map shows that the variability occurs within each particle but does not seem to be totally random. Pixel clusters of several tens of nanometers display relatively similar d-spacing values (Figure 8b). It may suggest that the process controlling the d-spacing was variable at the same spatial scale and that heterogeneously localized environmental conditions affected either the crystal chemistry, the organic matter nature, or their interactions.

CONCLUSION

Our study focuses on the detailed microstructural characterization of the phyllosilicates in Ryugu asteroid samples using 4D-STEM. Using advanced electron diffraction data analysis protocols, we characterized the mineralogy of Ryugu asteroid samples and identified the main minerals that are present. Our study identified Ni-bearing pyrrhotite in Ryugu, consistent with previous findings. We identified lizardite as the primary serpentine polymorph in Ryugu's matrix. If lizardite formed by the alteration of olivine, this alteration may have occurred at low temperatures. The main smectite reflection is located at an average distance of ~1.24 nm suggesting the presence of organic matter trapped within the interlayer space of smectite in addition to possible residual water molecules. The spatial mapping of the interlayer spacing of smectite highlights the sub-microscale heterogeneity of Ryugu and shows the close association of organics with smectite-type clay minerals. Our findings highlight the importance of continued investigation into the mineralogical, chemical, and structural properties of asteroidal and chondritic samples, and the significant role that advanced electron microscopy techniques such as 4D-STEM can play in enhancing our understanding of such objects.

Acknowledgments—The Hayabusa2 project has been developed and led by JAXA in collaboration with Deutsches Zentrum für Luft-und Raumfahrt (DLR) and Centre national d'études spatiales (CNES), and supported by NASA and Australian Space Agency

(ASA). We thank all the members of the Hayabusa2 project for their technical and scientific contributions. We thank Colin Ophus for helpful discussions. This work was carried out on the electron microscopy facility of the Advanced Characterization Platform of the Chevreul Institute, University of Lille—CNRS. It has been funded by I-SITE ULNE and the "Métropole Européenne de Lille" through the "TEM-Aster projet." The Chevreul Institute is thanked for its help in the development of this work through the CHEMACT project supported by the "Ministère de l'Enseignement Supérieur de la Recherche et de l'Innovation," the region "Hauts-de-France" and the "Métropole Européenne de Lille." We are very grateful to Ed Cloutis and another anonymous reviewer for their careful review of the paper.

Conflict of Interest Statement—As corresponding author, I hereby declare that all the co-authors have approved the paper and that no conflict of interest exist.

Data Availability Statement—The data that support the findings of this study are available from the corresponding author upon reasonable request.

Editorial Handling—Dr. Edward Anthony Cloutis

REFERENCES

Akai, J. 1982. High Resolution Electron Microscopic Characterization of Phyllosilicates and Finding of a New Type with 11A Structure in Yamato-74662. *National Institute Polar Research Memoirs* 25: 131–144.

Andreani, M., Grauby, O., Baronnet, A., and Muñoz, M. 2008. Occurrence, Composition and Growth of Polyhedral Serpentine. *European Journal of Mineralogy* 20: 159–171.

Bailey, S. W., ed. 1991. *Hydrous Phyllosilicates: Exclusive of Micas, 2. Print*. Washington, DC: Mineralogical Society of America.

Barber, D. J. 1981. Matrix Phyllosilicates and Associated Minerals in C2M Carbonaceous Chondrites. *Geochimica et Cosmochimica Acta* 45: 945–970. https://www.sciencedirect.com/science/article/pii/0016703781901204.

Béché, A., Rouvière, J. L., Clément, L., and Hartmann, J. M. 2009. Improved Precision in Strain Measurement Using Nanobeam Electron Diffraction. *Applied Physics Letters* 95: 123114. https://doi.org/10.1063/1.3224886.

Beck, P., Garenne, A., Quirico, E., Bonal, L., Montes-Hernandez, G., Moynier, F., and Schmitt, B. 2014. Transmission Infrared Spectra (2–25 μm) of Carbonaceous Chondrites (CI, CM, CV-CK, CR, C2 Ungrouped): Mineralogy, Water, and Asteroidal Processes. *Icarus* 229: 263–277. https://hal-insu.archives-ouvertes.fr/insu-03618604.

Berger, E. L., Lauretta, D. S., Zega, T. J., and Keller, L. P. 2016. Heterogeneous Histories of Ni-Bearing Pyrrhotite and Pentlandite Grains in the CI Chondrites Orgueil and Alais. *Meteoritics & Planetary Science* 51: 1813–29. https://doi.org/10.1111/maps.12721.

Brearley, A. J. 1995. Aqueous Alteration and Brecciation in Bells, an Unusual, Saponite-Bearing, CM Chondrite. *Geochimica et Cosmochimica Acta* 59: 2291–2317. https://www.sciencedirect.com/science/article/pii/001670379500107B.

Brearley, A. J. 2006. The Action of Water. In *Meteorites and the Early Solar System II*, edited by D. S. Lauretta, and H. Y. McSween, Jr., 584–624. Tucson, AZ: University of Arizona Press.

Brindley, G. W., and Brown, G. 1980. *Crystal Structures of Clay Minerals and their X-Ray Identification*. London: Mineralogical Society.

Bustillo, K. C., Zeltmann, S. E., Chen, M., Donohue, J., Ciston, J., Ophus, C., and Minor, A. M. 2021. 4D-STEM of Beam-Sensitive Materials. *Accounts of Chemical Research* 54: 2543–51. https://doi.org/10.1021/acs.accounts.1c00073.

Clayton, R. N., and Mayeda, T. K. 1984. The Oxygen Isotope Record in Murchison and Other Carbonaceous Chondrites. *Earth and Planetary Science Letters* 67: 151–161. https://www.sciencedirect.com/science/article/pii/0012821X84901109.

Colten-Bradley, V. A. 1987. Role of Pressure in Smectite Dehydration—Effects on Geopressure and Smectite-to-Illite Transformation. *AAPG Bulletin* 71: 1414–27. https://doi.org/10.1306/703C8092-1707-11D7-8645000102C1865D.

De la Peña, F., Prestat, E., Fauske, V. T., Burdet, P., Lähnemann, J., Jokubauskas, P., Furnival, T., et al. 2022. Hyperspy/Hyperspy: Release v1.7.1. https://zenodo.org/record/6659919.

Dobrică, E., Ishii, H. A., Bradley, J. P., Ohtaki, K., Brearley, A. J., Noguchi, T., Matsumoto, T., et al. 2023. Nonequilibrium Spherulitic Magnetite in the Ryugu Samples. *Geochimica et Cosmochimica Acta* 346: 65–75. https://www.sciencedirect.com/science/article/pii/S0016703723000674.

Ehrhardt, K. M., Radomsky, R. C., and Warren, S. C. 2021. Quantifying the Local Structure of Nanocrystals, Glasses, and Interfaces Using TEM-Based Diffraction. *Chemistry of Materials* 33: 8990–9011. https://doi.org/10.1021/acs.chemmater.1c03017.

Evans, B. W. 2004. The Serpentinite Multisystem Revisited: Chrysotile is Metastable. *International Geology Review* 46: 479–506. https://doi.org/10.2747/0020-6814.46.6.479.

Ferrage, E. 2016. Investigation of the Interlayer Organization of Water and Ions in Smectite from the Combined Use of Diffraction Experiments and Molecular Simulations. A Review of Methodology, Applications, and Perspectives. *Clays and Clay Minerals* 64: 348–373. https://doi.org/10.1346/CCMN.2016.0640401.

Ferrell, R. E., and Paulson, G. G. 1977. Practical Limitations of Selected Area Electron Diffraction Techniques for Identifying Mineral Particles. *Micron (1969)* 8: 47–55. https://doi.org/10.1016/0047-7206(77)90009-7.

Gammer, C., Burak, O. V., Liebscher, C. H., and Minor, A. M. 2015. Diffraction Contrast Imaging Using Virtual Apertures. *Ultramicroscopy* 155: 1–10. https://www.sciencedirect.com/science/article/pii/S0304399115000649.

Gemmi, M., and Lanza, A. E. 2019. 3D Electron Diffraction Techniques. *Acta Crystallographica Section B* 75: 495–504.

Harisson, C. S., King, A. J., Jones, R. H., Russell, S. S., Nakamura, T., Yurimoto, H., Noguchi, T., et al. 2022. Fe-

Sulfides in Ryugu Particle C0025-01: A Comparison with CI and CY Chondrites. *Proceedings, 85th Annual Meeting of the Meteoritical Society*.

Howard, K. T., Benedix, G. K., Bland, P. A., and Cressey, G. 2009. Modal Mineralogy of CM2 Chondrites by X-Ray Diffraction (PSD-XRD). Part 1: Total Phyllosilicate Abundance and the Degree of Aqueous Alteration. *Geochimica et Cosmochimica Acta* 73: 4576–89. https://www.sciencedirect.com/science/article/pii/S0016703709003007.

Howard, K. T., Benedix, G. K., Bland, P. A., and Cressey, G. 2011. Modal Mineralogy of CM Chondrites by X-Ray Diffraction (PSD-XRD): Part 2. Degree, Nature and Settings of Aqueous Alteration. *Geochimica et Cosmochimica Acta* 75: 2735–51. https://www.sciencedirect.com/science/article/pii/S0016703711001001.

Im, S., Chen, Z., Johnson, J. M., Zhao, P., Yoo, G. H., Park, E. S., Wang, Y., Muller, D. A., and Hwang, J. 2018. Direct Determination of Structural Heterogeneity in Metallic Glasses Using Four-Dimensional Scanning Transmission Electron Microscopy. *Ultramicroscopy* 195: 189–193. https://www.sciencedirect.com/science/article/pii/S030439911830158X.

Ito, M., Tomioka, N., Uesugi, M., Yamaguchi, A., Shirai, N., Ohigashi, T., Liu, M. C., et al. 2022. A Pristine Record of Outer Solar System Materials from Asteroid Ryugu's Returned Sample. *Nature Astronomy* 6: 1163–71. https://www.nature.com/articles/s41550-022-01745-5.

King, A. J., Schofield, P. F., Howard, K. T., and Russell, S. S. 2015. Modal Mineralogy of CI and CI-Like Chondrites by X-Ray Diffraction. *Geochimica et Cosmochimica Acta* 165: 148–160. https://www.sciencedirect.com/science/article/pii/S0016703715003634.

King, A. J., Schofield, P. F., and Russell, S. S. 2017. Type 1 Aqueous Alteration in CM Carbonaceous Chondrites: Implications for the Evolution of Water-Rich Asteroids. *Meteoritics & Planetary Science* 52: 1197–1215. https://doi.org/10.1111/maps.12872.

Krajnak, M., McGrouther, D., Maneuski, D., Shea, V. O., and McVitie, S. 2016. Pixelated Detectors and Improved Efficiency for Magnetic Imaging in STEM Differential Phase Contrast. *Ultramicroscopy* 165: 42–50. https://www.sciencedirect.com/science/article/pii/S0304399116300183.

Lagaly, G., and Beneke, K. 1991. Intercalation and Exchange Reactions of Clay Minerals and Non-Clay Layer Compounds. *Colloid and Polymer Science* 269: 1198–1211. https://doi.org/10.1007/BF00652529.

Lanson, B., Mignon, P., Velde, M., Bauer, A., Lanson, M., Findling, N., and Perez del Valle, C. 2022. Determination of Layer Charge Density in Expandable Phyllosilicates with Alkylammonium Ions: A Combined Experimental and Theoretical Assessment of the Method. *Applied Clay Science* 229: 106665. https://www.sciencedirect.com/science/article/pii/S0169131722002605.

Lauretta, D. S., Hua, X., and Buseck, P. R. 2000. Mineralogy of Fine-Grained Rims in the Alh 81002 cm Chondrite. *Geochimica et Cosmochimica Acta* 64: 3263–73. https://www.sciencedirect.com/science/article/pii/S0016703700004257.

Le Guillou, C., Remusat, L., Bernard, S., Brearley, A. J., and Leroux, H. 2013. Amorphization and D/H Fractionation of Kerogens during Experimental Electron Irradiation: Comparison with Chondritic Organic Matter. *Icarus* 226: 101–110. https://www.sciencedirect.com/science/article/pii/S0019103513002030.

Leroux, H., Le Guillou, C., Marinova, M., Laforet, S., Viennet, J. C., Mouloud, B. E., Teurtrie, A., et al. Forthcoming. Phyllosilicates with Embedded Fe-Based Nanophases in Ryugu 2 and Orgueil. *Meteoritics & Planetary Sciences*. Submitted for publication.

Li, P., and Egerton, R. 2003. Electron Irradiation Damage to Aromatic Compounds. *Microscopy and Microanalysis* 9: 986–87. https://doi.org/10.1017/S1431927603444930.

Li, G., Zhang, H., and Han, Y. 2022. 4D-STEM Ptychography for Electron-Beam-Sensitive Materials. *ACS Central Science* 8: 1579–88. https://doi.org/10.1021/acscentsci.2c01137.

MacKinnon, I. D. R. 1980. Structures and Textures of the Murchison and Mighei Carbonaceous Chondrite Matrices. *11th Lunar and Planetary Science Conference*, Houston, TX, March 17–21 2: 839–852.

Marinova, M., Leroux, H., Cuvillier, P., Gloter, A., and Jacob, D. 2021. STEM-EELS Investigation of Planar Defects in Olivine in the Allende Meteorite. *Minerals* 11: 35. https://www.mdpi.com/2075-163X/11/1/35.

Mellini, M. 2013. Structure and Microstructure of Serpentine Minerals. *Minerals at the Nanoscale*: 153–179. https://doi.org/10.1180/emu-notes.14.5.

Mellini, M., Cressey, G., Wicks, F. J., and Cressey, B. A. 2010. The Crystal Structure of Mg End-Member Lizardite-1 T Forming Polyhedral Spheres from the Lizard, Cornwall. *Mineralogical Magazine* 74: 277–284.

Moyano, B., Spikes, K. T., Johansen, T. A., and Mondol, N. H. 2012. Modeling Compaction Effects on the Elastic Properties of Clay-Water Composites. *Geophysics* 77: D171–D183. https://doi.org/10.1190/geo2011-0426.1.

Nakamura, T., Matsumoto, M., Amano, K., Enokido, Y., Zolensky, M. E., Mikouchi, T., Genda, H., et al. 2023. Formation and Evolution of Carbonaceous Asteroid Ryugu: Direct Evidence from Returned Samples. *Science* 379: eabn8671.

Nakano, A., Tokonami, M., and Morimoto, N. 1979. Refinement of 3C Pyrrhotite, Fe7S8. *Acta Crystallographica Section B* 35: 722–24.

Noguchi, T., Matsumoto, T., Miyake, A., Igami, Y., Haruta, M., Saito, H., Hata, S., et al. 2023. A Dehydrated Space-Weathered Skin Cloaking the Hydrated Interior of Ryugu. *Nature Astronomy* 7: 170–181. https://www.nature.com/articles/s41550-022-01841-6.

Noguchi, T., Matsumoto, T., Miyake, A., Igami, Y., Haruta, M., Saito, H., Hata, S., et al. Forthcoming. Mineralogy and Petrology of Fine-Grained Samples Recovered from the Asteroid (162173) Ryugu. *Meteoritics & Planetary Sciences*. Submitted for publication.

O'Hanley, D. S., Chernosky, J. V., and Wicks, F. J. 1989. The Stability of Lizardite and Chrysotile. *The Canadian Mineralogist* 27: 483–493.

O'Hanley, D. S., and Wicks, F. J. 1995. Conditions of Formation of Lizardite, Chrysotile and Antigorite, Cassiar, British Columbia. *The Canadian Mineralogist* 33: 753–773.

Ophus, C. 2019. Four-Dimensional Scanning Transmission Electron Microscopy (4D-STEM): From Scanning Nanodiffraction to Ptychography and beyond. *Microscopy and Microanalysis* 25: 563–582.

Ophus, C., Zeltmann, S. E., Bruefach, A., Rakowski, A., Savitzky, B. H., Minor, A. M., and Scott, M. C. 2022. Automated Crystal Orientation Mapping in py4DSTEM Using Sparse Correlation Matching. *Microscopy and Microanalysis* 28: 390–403. http://arxiv.org/abs/2111.00171.

Osawa, T., Kagi, H., Nakamura, T., and Noguchi, T. 2005. Infrared Spectroscopic Taxonomy for Carbonaceous Chondrites from Speciation of Hydrous Components. *Meteoritics & Planetary Science* 40: 71–86. https://doi.org/10.1111/j.1945-5100.2005.tb00365.x.

Palatinus, L., Correa, C. A., Steciuk, G., Jacob, D., Roussel, P., Boullay, P., Klementova, M., et al. 2015. Structure Refinement Using Precession Electron Diffraction Tomography and Dynamical Diffraction: Tests on Experimental Data. *Acta Crystallographica Section B* 71: 740–751.

Palatinus, L., Petricek, V., and Correa, C. A. 2015. Structure Refinement Using Precession Electron Diffraction Tomography and Dynamical Diffraction: Theory and Implementation. *Acta Crystallographica Section A* 71: 235–244.

Paterson, G. W., Webster, R. W. H., Ross, A., Paton, K. A., Macgregor, T. A., Mc-Grouther, D., MacLaren, I., and Nord, M. 2020. Fast Pixelated Detectors in Scanning Transmission Electron Microscopy. Part II: Post-Acquisition Data Processing, Visualization, and Structural Characterization. *Microscopy and Microanalysis* 26: 944–963. https://doi.org/10.1017/S1431927620024307.

Pennycook, T. J., Martinez, G. T., Nellist, P. D., and Meyer, J. C. 2019. High Dose Efficiency Atomic Resolution Imaging Via Electron Ptychography. *Ultramicroscopy* 196: 131–35. https://www.sciencedirect.com/science/article/pii/S0304399118302316.

Pignatelli, I., Mugnaioli, E., and Marrocchi, Y. 2018. Cronstedtite Polytypes in the Paris Meteorite. *European Journal of Mineralogy* 30: 349–354.

Plackett, R., Horswell, I., Gimenez, E. N., Marchal, J., Omar, D., and Tartoni, N. 2013. Merlin: A Fast Versatile Readout System for Medipix3. *Journal of Instrumentation* 8: C01038. https://doi.org/10.1088/1748-0221/8/01/C01038.

Rajamani, V., and Prewitt, C. T. 1975. Thermal Expansion of the Pentlandite Structure. *American Mineralogist* 60: 39–48.

Rondeau, B., Devouard, B., Jacob, D., Roussel, P., Stephant, N., Boulet, C., Mollé, V., et al. 2019. Lasnierite, (Ca,Sr)$(Mg,Fe)_2Al(PO4)_3$, a New Phosphate Accompanying Lazulite from Mt. Ibity, Madagascar: An Example of Structural Characterization from Dynamical Refinement of Precession Electron Diffraction Data on Submicrometre Sample. *European Journal of Mineralogy* 31: 379–388.

Savitzky, B. H., Zeltmann, S. E., Hughes, L. A., Brown, H. G., Zhao, S., Pelz, P. M., Pekin, T. C., et al. 2021. py4DSTEM: A Software Package for Four-Dimensional Scanning Transmission Electron Microscopy Data Analysis. *Microscopy and Microanalysis* 27: 712–743.

Sayers, C. M., and den Boer, L. D. 2016. The Elastic Anisotropy of Clay Minerals. *Geophysics* 81: C193–C203. https://doi.org/10.1190/geo2016-0005.1.

Schrader, D. L., Davidson, J., McCoy, T. J., Zega, T. J., Russell, S. S., Domanik, K. J., and King, A. J. 2021. The Fe/S Ratio of Pyrrhotite Group Sulfides in Chondrites: An Indicator of Oxidation and Implications for Return Samples from Asteroids Ryugu and Bennu. *Geochimica et Cosmochimica Acta* 303: 66–91. https://www.sciencedirect.com/science/article/pii/S001670372100185X.

Schwartz, S., Guillot, S., Reynard, B., Lafay, R., Debret, B., Nicollet, C., Lanari, P., and Auzende, A. L. 2013. Pressure–Temperature Estimates of the Lizardite/Antigorite Transition in High Pressure Serpentinites. *Lithos* 178: 197–210. https://www.sciencedirect.com/science/article/pii/S0024493712004781.

Stroud, R. M., Barosch, J., Bonal, L., Burgess, K., Cody, G. D., De Gregorio, B. T., Daly, L., et al. Forthcoming. Electron Microscopy Observations of the Diversity of Ryugu Organic Matter and its Relationship to Minerals at the Micro-to-Nanoscale. *Meteoritics & Planetary Sciences*. Submitted for publication.

Tachibana, S., Sawada, H., Okazaki, R., Takano, Y., Sakamoto, K., Miura, Y. N., Okamoto, C., et al. 2022. Pebbles and Sand on Asteroid (162173) Ryugu: In Situ Observation and Particles Returned to Earth. *Science* 375: 1011–16. https://doi.org/10.1126/science.abj8624.

Takir, D., Emery, J. P., Mcsween, H. Y., Jr., Hibbitts, C. A., Clark, R. N., Pearson, N., and Wang, A. 2013. Nature and Degree of Aqueous Alteration in CM and CI Carbonaceous Chondrites. *Meteoritics & Planetary Science* 48: 1618–37. https://doi.org/10.1111/maps.12171.

Tate, M. W., Purohit, P., Chamberlain, D., Nguyen, K. X., Hovden, R., Chang, C. S., Deb, P., et al. 2016. High Dynamic Range Pixel Array Detector for Scanning Transmission Electron Microscopy. *Microscopy and Microanalysis* 22: 237–249. https://doi.org/10.1017/S1431927615015664.

Tomeoka, K., and Buseck, P. R. 1985. Indicators of Aqueous Alteration in CM Carbonaceous Chondrites: Microtextures of a Layered Mineral Containing Fe, S, O and Ni. *Geochimica et Cosmochimica Acta* 49: 2149–63.

Tomeoka, K., and Buseck, P. R. 1988. Matrix Mineralogy of the Orgueil CI Carbonaceous Chondrite. *Geochimica et Cosmochimica Acta* 52: 1627–40. https://www.sciencedirect.com/science/article/pii/0016703788902311.

Trigo-Rodríguez, J. M., Rimola, A., Tanbakouei, S., Soto, V. C., and Lee, M. 2019. Accretion of Water in Carbonaceous Chondrites: Current Evidence and Implications for the Delivery of Water to Early Earth. *Space Science Reviews* 215: 18. https://doi.org/10.1007/s11214-019-0583-0.

Uehara, S. 1998. TEM and XRD Study of Antigorite Superstructures. *The Canadian Mineralogist* 36: 1595–1605.

Vance, S. D., and Melwani, D. M. 2020. Serpentinite and the Search for Life beyond Earth. *Philosophical Transactions of the Royal Society A: Mathematical, Physical and Engineering Sciences* 378: 20180421. https://doi.org/10.1098/rsta.2018.0421.

Viennet, J.-C., Bernard, S., Le Guillou, C., Jacquemot, P., Balan, E., Delbes, L., Rigaud, B., Georgelin, T., and Jaber, M. 2019. Experimental Clues for Detecting Biosignatures on Mars. *Geochemical Perspectives Letters* 12: 28–33.

Viennet, J.-C., Bernard, S., Le Guillou, C., Jacquemot, P., Delbes, L., Balan, E., and Jaber, M. 2020. Influence of the Nature of the Gas Phase on the Degradation of RNA during Fossilization Processes. *Applied Clay Science* 191: 105616. https://www.sciencedirect.com/science/article/pii/S0169131720301812.

Viennet, J.-C., Bernard, S., Le Guillou, C., Sautter, V., Grégoire, B., Jambon, A., Pont, S., et al. 2021. Martian Magmatic Clay Minerals Forming Vesicles: Perfect Niches for Emerging Life? *Astrobiology* 21: 605–612. https://doi.org/10.1089/ast.2020.2345.

Viennet, J.-C., Le Guillou, C., Remusat, L., Baron, F., Delbes, L., Blanchenet, A. M., Laurent, B., Criouet, I., and Bernard, S. 2022. Experimental Investigation of Fe-Clay/Organic Interactions under Asteroidal Conditions. *Geochimica et Cosmochimica Acta* 318: 352–365. https://www.sciencedirect.com/science/article/pii/S0016703721006967.

Viennet, J. C., Roskosz, M., Nakamura, T., Beck, P., Baptiste, B., Lavina, B., Alp, E. E., et al. 2023. Interaction between Clay Minerals and Organics in Asteroid Ryugu. *Geochemical Perspectives Letters* 25: 8–12.

Wenner, D. B., and Taylor, H. P. 1971. Temperatures of Serpentinization of Ultramafic Rocks Based on O^{18}/O^{16} Fractionation between Coexisting Serpentine and Magnetite. *Contributions to Mineralogy and Petrology* 32: 165–185. https://doi.org/10.1007/BF00643332.

Yabuta, H., Cody, G. D., Engrand, C., Kebukawa, Y., de Gregorio, B., Bonal, L., Remusat, L., et al. 2023. Macromolecular Organic Matter in Samples of the Asteroid (162173) Ryugu. *Science* 379: eabn9057. https://doi.org/10.1126/science.abn9057.

Yada, K. 1971. Study of Microstructure of Chrysotile Asbestos by High-Resolution Electron Microscopy. *Acta Crystallographica Section A* 27: 659–664. https://doi.org/10.1107/s0567739471001402.

Yada, T., Abe, M., Okada, T., Nakato, A., Yogata, K., Miyazaki, A., Hatakeda, K., et al. 2022. Preliminary Analysis of the Hayabusa2 Samples Returned from C-Type Asteroid Ryugu. *Nature Astronomy* 6: 214–220. https://www.nature.com/articles/s41550-021-01550-6.

Yamaguchi, A., Tomioka, N., Ito, M., Shirai, N., Kimura, M., Greenwood, R. C., Liu, M. C., et al. 2023. Insight into Multi-Step Geological Evolution of C-Type Asteroids from Ryugu Particles. *Nature Astronomy* 7: 398–405.

Yang, H., Ercius, P., Nellist, P. D., and Ophus, C. 2016. Enhanced Phase Contrast Transfer Using Ptychography Combined with a Pre-Specimen Phase Plate in a Scanning Transmission Electron Microscope. *Ultramicroscopy* 171: 117–125. https://www.sciencedirect.com/science/article/pii/S0304399116301966.

Yang, H., MacLaren, I., Jones, L., Martinez, G. T., Simson, M., Huth, M., Ryll, H., et al. 2017. Electron Ptychographic Phase Imaging of Light Elements in Crystalline Materials Using Wigner Distribution Deconvolution. *Ultramicroscopy* 180: 173–79. https://www.sciencedirect.com/science/article/pii/S0304399117300773.

Yi, F., and Voyles, P. M. 2011. Effect of Sample Thickness, Energy Filtering, and Probe Coherence on Fluctuation Electron Microscopy Experiments. *Ultramicroscopy* 111: 1375–80. https://www.sciencedirect.com/science/article/pii/S030439911100163X.

Yokoyama, T., Nagashima, K., Nakai, I., Young, E. D., Abe, Y., Aléon, J., Alexander, C. M., et al. 2022. Samples Returned from the Asteroid Ryugu are Similar to Ivuna-Type Carbonaceous Meteorites. *Science* 379: eabn7850. https://doi.org/10.1126/science.abn7850.

Zega, T. J., Garvie, L. A. J., Dódony, I., Friedrich, H., Stroud, R. M., and Buseck, P. R. 2006. Polyhedral Serpentine Grains in CM Chondrites. *Meteoritics & Planetary Science* 41: 681–88. https://doi.org/10.1111/j.1945-5100.2006.tb00984.x.

Zvyagin, B. B. 1967. *Electron-Diffraction Analysis of Clay Mineral Structures*. Boston, MA: Springer US. https://doi.org/10.1007/978-1-4615-8612-8.